

EXPERIMENTAL INVESTIGATION OF BOUNDARY LAYER SEPARATION
CONTROL USING STEADY VORTEX GENERATOR JETS ON LOW
PRESSURE TURBINES

A THESIS SUBMITTED TO
THE GRADUATE SCHOOL OF NATURAL AND APPLIED SCIENCES
OF
MIDDLE EAST TECHNICAL UNIVERSITY

BY

EDA DOĞAN

IN PARTIAL FULFILLMENT OF THE REQUIREMENTS
FOR
THE DEGREE OF MASTER OF SCIENCE
IN
AEROSPACE ENGINEERING

JUNE 2012

Approval of the thesis:

**EXPERIMENTAL INVESTIGATION OF BOUNDARY LAYER
SEPARATION CONTROL USING STEADY VORTEX GENERATOR JETS
ON LOW PRESSURE TURBINES**

submitted by **EDA DOĞAN** in partial fulfillment of the requirements for the degree
of **Master of Science in Aerospace Engineering Department, Middle East
Technical University** by,

Prof. Dr. Canan ÖZGEN
Dean, Graduate School of **Natural and Applied Sciences**

Prof. Dr. Ozan TEKİNALP
Head of Department, **Aerospace Engineering**

Assist. Prof. Dr. Oğuz UZOL
Supervisor, **Aerospace Engineering Dept., METU**

Assoc. Prof. Dr. Dilek Funda KURTULUŞ
Co-Supervisor, **Aerospace Engineering Dept., METU**

Examining Committee Members:

Prof. Dr. Yusuf ÖZYÖRÜK
Aerospace Engineering Dept., METU

Assist. Prof. Dr. Oğuz UZOL
Aerospace Engineering Dept., METU

Prof. Dr. İsmail Hakkı TUNCER
Aerospace Engineering Dept., METU

Prof. Dr. Serkan ÖZGEN
Aerospace Engineering Dept., METU

Dr. Barış GÜMÜŞEL
Compressor Module Design Leader, TEI

Date: 27.06.2012

I hereby declare that all information in this document has been obtained and presented in accordance with academic rules and ethical conduct. I also declare that, as required by these rules and conduct, I have fully cited and referenced all material and results that are not original to this work.

Name, Last Name : Eda Dođan

Signature :

ABSTRACT

EXPERIMENTAL INVESTIGATION OF BOUNDARY LAYER SEPARATION CONTROL USING STEADY VORTEX GENERATOR JETS ON LOW PRESSURE TURBINES

Doğan, Eda

M.Sc., Department of Aerospace Engineering

Supervisor : Assist. Prof. Dr. Oğuz Uzol

Co-Supervisor: Assoc. Prof. Dilek Funda Kurtuluş

June 2012, 64 Pages

This thesis presents the results of an experimental study that investigates the effects of steady vortex generator jets (VGJs) integrated to a low pressure turbine blade to control the laminar separation bubble occurring on the suction surface of the blade at low Reynolds numbers. The injection technique involves jets issued from the holes located near the suction peak of the test blade which is in the middle of a five-blade low speed linear cascade facility. Three injection cases are tested with different blowing ratio values ranging from low to high. Surface pressure and particle image velocimetry (PIV) measurements are performed. The results show that steady VGJ is effective in eliminating the laminar separation bubble. Also it is observed that to have fully developed attached boundary layer, blowing ratio should be chosen accordingly since a very thin separation zone still exists at low blowing ratios.

Keywords: Active Flow Control, Laminar Separation Bubble, Steady Vortex Generator Jet, Low Pressure Turbine Cascade.

ÖZ

DAİMİ GİRDAP ÜRETİCİ JET KULLANARAK DÜŞÜK BASINÇLI TÜRBİN ÜZERİNDE SINIR TABAKASI AYRILMASI KONTROLÜNÜN DENEYSEL İNCELENMESİ

Doğan, Eda

Yüksek Lisans, Havacılık ve Uzay Mühendisliği Bölümü

Tez Yöneticisi : Yrd. Doç. Dr. Oğuz Uzol

Ortak Tez Yöneticisi : Doç. Dr. Dilek Funda Kurtuluş

Haziran 2012, 64 sayfa

Bu çalışma, düşük Reynolds sayılı akışlarda düşük basınçlı türbin kanadının emme yüzeyinde oluşan laminer ayrılma baloncuğunun kontrolünde daimi girdap üretici jet üfleme metodunun etkinliğinin deneysel olarak incelenmesinin sonuçlarını sunmaktadır. Üfleme metodu beş kanattan oluşan düşük hızlı bir kaskat düzeneğinin ortasındaki test kanadı üzerine, kanadın en düşük basınç noktası göz önüne alınarak yerleştirilmiştir. Düşükten yükseğe üç farklı üfleme katsayısı ile çalışılmıştır. Kanat yüzeyi basınç ölçümü ve Parçacık İmge Hızölçer metotları kullanılmıştır. Sonuçlar, laminer akım baloncuğunun yok edildiğini göstermektedir. Düşük hızlı üflemelelerde çok ince olsa da bir ayrılma bölgesi gözlemlendiği için tam gelişmiş yüzeye yapışık bir sınır tabakası isteniyorsa üfleme katsayısı seçimi uygun bir şekilde yapılmalıdır.

Anahtar Kelimeler: Aktif Akış Kontrolü, Laminer Ayrılma Baloncuğu, Daimi Girdap Üretici Jet, Düşük Basınçlı Türbin Kaskatı

To my parents and my sister

ACKNOWLEDGMENTS

I would like to express my deepest gratitude to my supervisor Dr. Oğuz Uzol for his guidance through this subject and for all the opportunities he provided to me to realize this study. Also to my co-supervisor Dr. Funda Kurtuluş for her support during my graduate studies. I am indebted to the technical support that our technicians, Murat Ceylan and Ahmet Uyar, provided to me. I am grateful to Bilgin Çelik for sharing his precious time for the design of the turbine blade. I am grateful to my colleagues Senem Ayşe Haser, Ezgi Anık, Melika Gül and Anas Abdulrahim for the long, exhausting experiment days with full of invaluable discussions on the study. As for my teammate Bayram Mercan, I am heartily thankful for his friendship and his support throughout my graduate years. I also would like to thank Dr. Stamatios Pothos of TSI Inc. for all the instructions and endless support. The one I owe too much is Prof. Dr. Cahit Çıray. I am truly indebted to him for giving me the confidence for success. I am heartily grateful for his precious contributions to my graduate years. I would like to thank Çağıl Türeli and Tuğçe Karabacak to support me for time-consuming parts of this study apart from being my dearest friends and I am also thankful to all my precious friends for their existence in my life during those hard-working days.

Last, but not least, I owe my sincere thanks to my dear parents, Ayten and Kemal Doğan and to my dearest sister, Emel Doğan Kurtoğlu, for their endless love, faith, patience and support throughout my life. Their being my family is the first reason for being motivated for all the aims in my life. I also would like to express my deepest thanks to Muhit for his presence in my life with all his love, assistance and encouragement and always being after what I am doing.

TABLE OF CONTENTS

ABSTRACT.....	iv
ÖZ	v
ACKNOWLEDGMENTS	vii
TABLE OF CONTENTS.....	viii
LIST OF TABLES	x
LIST OF FIGURES	xi
NOMENCLATURE.....	xiv
CHAPTERS	
1. INTRODUCTION	1
1.1 Literature Survey.....	3
1.1.1 Low Pressure Turbine Boundary Layer Separation.....	3
1.1.2 Low Pressure Turbine Boundary Layer Separation Control.....	5
1.2 Objectives and Contents of the Study	8
2. EXPERIMENTAL PROCEDURE	10
2.1 Experimental Setup	10
2.1.1 Low-Speed Cascade Wind Tunnel.....	10
2.1.2 Cascade Test Section.....	11
2.1.3 Vortex Generator Jet (VGJ) Configuration.....	13
2.2 Measurement Details.....	16
2.2.1 Surface Pressure Measurements.....	16
2.2.2 Total Pressure Measurements	18

2.2.3	2D Particle Image Velocimetry (PIV) Measurements	19
2.2.4	Injection Scenarios	23
2.2.5	Uncertainty Estimates	24
3.	EXPERIMENTAL RESULTS AND DISCUSSION.....	26
3.1	Baseline Case (B=0).....	26
3.1.1	Surface Pressure Measurement Results	28
3.1.2	2D Particle Image Velocimetry Measurement Results	29
3.2	Steady Vortex Generator Jet (VGJ) Cases.....	46
4.	CONCLUSION.....	59
4.1	General Conclusions	59
4.2	Recommendations for Further Research.....	60
	REFERENCES.....	61

LIST OF TABLES

TABLES

Table 2.1.1: Specifications of T106 cascade.....	12
Table 2.2.1: Pressure tap locations.....	17
Table 2.2.2: Steady blowing cases	24

LIST OF FIGURES

FIGURES

Figure 1.1: LP turbine airfoil count trend [4].....	2
Figure 1.1.1: Total pressure losses vs. Reynolds number [5]	3
Figure 1.1.2: Schematic view of the development of laminar separated boundary layer with associated pressure distribution [3].....	4
Figure 1.1.3: Schematic of VGJ, α : pitch angle, β : skew angle [11]	6
Figure 2.1.1: Sketch of Active Flow Control Wind Tunnel [18].....	11
Figure 2.1.2: Fully transparent test section mounted at the exit of the contraction section	12
Figure 2.1.3: The fluidic oscillator geometry and its specifications [20]	13
Figure 2.1.4: The consecutive snapshots of the video taken during the experiment .	14
Figure 2.1.5: The solid model of the oscillator integrated test blade.....	14
Figure 2.1.6: Fluidic oscillator integrated turbine blade in two pieces to be glued ...	15
Figure 2.2.1: Pressure tapped blade	17
Figure 2.2.2: Total pressure measurement line, top view (left), 3-D view (right).....	18
Figure 2.2.3: (a) PIV experimental setup (b) sketch of the test section with laser sheet	20
Figure 2.2.4: Sketch of measurement planes, LE: Leading Edge, TE: Trailing Edge	21
Figure 2.2.5: Sketch of PIV measurement plane and windows	22
Figure 2.2.6: Description of the jet injection	24
Figure 3.1.1: In-plane velocity magnitude/ U_∞ contours for (a) $Re=29k$ (b) $Re=58k$, $B=0$	27
Figure 3.1.2: Surface C_p distribution. $Re=29k$, $B=0$	28

Figure 3.1.3: In-plane mean velocity magnitude/ U_∞ contours at $z/d=0$ showing the aft portion of the blade (55% SSL-Trailing Edge (TE)). The flow is from left to right, $B=0$ and $Re=29k$	30
Figure 3.1.4: Turbulent kinetic energy/ U_∞^2 contours at $z/d=0$ showing the aft portion of the blade (55% SSL-Trailing Edge (TE)). The flow is from left to right, $B=0$ and $Re=29k$	31
Figure 3.1.5: Non-dimensional mean vorticity, $\Omega_z/(U_\infty/C_x)$, contours at $z/d=0$ showing the aft portion of the blade (55% SSL-Trailing Edge (TE)). The flow is from left to right, $B=0$ and $Re=29k$	32
Figure 3.1.6: $-u'v'/U_\infty^2$ contours at $z/d=0$ showing the aft portion of the blade (55% SSL-Trailing Edge (TE)). The flow is from left to right, $B=0$ and $Re=29k$	33
Figure 3.1.7: Instantaneous in-plane velocity magnitude/ U_∞ contours at $z/d=0$ showing the regions (a) 95% SSL- TE (b) 85% SSL-95% SSL (c) 75% SSL- 85% SSL (d) 65% SSL-75% SSL (e) 55% SSL- 65% SSL. The flow is from bottom to top, $B=0$ and $Re=29k$	34
Figure 3.1.8: Instantaneous vorticity (Ω_z)/(U_∞/C_x) contours at $z/d=0$ showing the regions (a) 95% SSL- TE (b) 85% SSL-95% SSL (c) 75% SSL- 85% SSL (d) 65% SSL-75% SSL (e) 55% SSL- 65% SSL. The flow is from bottom to top, $B=0$ and $Re=29k$	35
Figure 3.1.9: Coordinate systems and specified SSL stations	37
Figure 3.1.10: Boundary layer profiles of mean streamwise velocity normalized by local edge velocity; profiles at different s/SSL stations at $z/d=0$, $B=0$, $Re=29k$	38
Figure 3.1.11: Laminar separation bubble obtained from velocity profiles.....	40
Figure 3.1.12: Displacement and momentum thickness values at different s/SSL stations at $z/d=0$, $B=0$, $Re=29k$	41
Figure 3.1.13: Shape factor values at different s/SSL stations at $z/d=0$, $B=0$, $Re=29k$	42
Figure 3.1.14: Normalized Reynolds stress components at specified SSL locations (a) Reynolds normal stresses, $u'_n u'_n / U_e^2$ (b) Reynolds normal stresses, $u'_s u'_s / U_e^2$, (c) Reynolds shear stresses, $-u'_s u'_n / U_e^2$. At $z/d=0$, $B=0$, $Re=29k$	44

Figure 3.2.1: In-plane mean velocity magnitude/ U_∞ contours at $z/d=0$ showing the aft portion of the blade (55% SSL-Trailing Edge (TE)). (a) $B=0$ (b) $B=2.2$ (c) $B=4.4$ (d) $B=7.2$. The flow is from left to right, $Re=29k$	47
Figure 3.2.2: Turbulent kinetic energy/ U_∞^2 contours at $z/d=0$ showing the aft portion of the blade (55% SSL-Trailing Edge (TE)). (a) $B=0$ (b) $B=2.2$ (c) $B=4.4$ (d) $B=7.2$. The flow is from left to right, $Re=29k$	49
Figure 3.2.3: $-\mathbf{u}'\mathbf{v}'/U_\infty^2$ contours at $z/d=0$ showing the aft portion of the blade (55% SSL-Trailing Edge (TE)). (a) $B=0$ (b) $B=2.2$ (c) $B=4.4$ (d) $B=7.2$. The flow is from left to right, $Re=29k$	50
Figure 3.2.4: Non-dimensional mean vorticity, $\Omega_z/(U_\infty/C_x)$, contours at $z/d=0$ showing the aft portion of the blade (55% SSL-Trailing Edge (TE)). (a) $B=0$ (b) $B=2.2$ (c) $B=4.4$ (d) $B=7.2$. The flow is from left to right, $Re=29k$	51
Figure 3.2.5: Non-dimensional mean vorticity, $\Omega_z/(U_\infty/C_x)$, contours showing the aft portion of the blade (55% SSL-Trailing Edge (TE)). (a) $z/d=0, B=0$. Injection cases ((b), (c), (d)) are at $B=2.2$. (b) $z/d=0$ (c) $z/d=12.5$ (d) $z/d=25$. The flow is from left to right, $Re=29k$	52
Figure 3.2.6: Boundary layer profiles of mean streamwise velocity normalized by mean edge velocity; profiles at different s/SSL stations at $z/d=0$ for (a) $B=2.2$, (b) $B=4.4$, (c) $B=7.2$, $Re=29k$	54
Figure 3.2.7: Displacement and momentum thickness comparison at $z/d=0$, $Re=29k$	56
Figure 3.2.8: Shape factor comparison for $B=0$ and $B=2.2$ at $z/d=0$, $Re=29k$	57
Figure 3.2.9: Pitchwise total pressure loss coefficient variation at midspan, $0.5C_x$ downstream of the blade row for baseline ($B=0$) and three injection cases	58

NOMENCLATURE

b	Blade span [mm]
B	Blowing ratio, $B = \frac{U_j}{U_\infty}$
C_p	Pressure coefficient, $C_p = \frac{P_{01} - P_s}{P_{01} - P_{2s}}$
$C_{p,loss}$	Total pressure loss coefficient, $C_{p,loss} = \frac{P_t - P_{01}}{0.5\rho U_\infty^2}$
C_x	Axial chord [mm]
d	Hole diameter [mm]
LE	Leading Edge
LPT	Low Pressure Turbine
P_{01}	Cascade inlet total pressure
P_s	Measured local static pressure
P_{2s}	Cascade exit static pressure
P_t	Measured local total pressure
PIV	Particle Image Velocimetry
Re	Reynolds number based on cascade inlet velocity and axial chord
s	Blade pitch [mm]
SSL	Suction Surface Length
TE	Trailing Edge
TKE	Turbulent Kinetic Energy
U_e	Local edge velocity [m/s]
U_j	Mean jet velocity [m/s]
U_∞	Free stream inlet velocity [m/s]
U_s	Streamwise velocity [m/s]

$\overline{u'_n u'_n}$	Reynolds normal stress per unit mass in blade-normal direction [m ² /s ²]
$\overline{u'_s u'_s}$	Reynolds normal stress per unit mass in streamwise direction [m ² /s ²]
$-\overline{u'_s u'_n}$	Reynolds shear stress per unit mass [m ² /s ²]
<i>VGJ</i>	Vortex Generator Jet
<i>Zweifel coefficient</i>	$\frac{s(\tan\alpha_2 - \tan\alpha_1)}{0.5C_x \sec^2\alpha_2}$
α	VGJ pitch angle
α_1	Blade inlet flow angle [deg]
α_2	Blade exit flow angle [deg]
β	VGJ skew angle [deg]
δ^*	Displacement thickness, $\delta^* = \int_0^\infty \left(1 - \frac{u_s}{u_e}\right) dy$
θ	Momentum thickness, $\theta = \int_0^\infty \frac{u_s}{u_e} \left(1 - \frac{u_s}{u_e}\right) dy$
Δt	Laser pulse separation time [μ s]
ρ	Inlet flow density [kg/m ³]

CHAPTER 1

INTRODUCTION

Low pressure turbine (LPT) is an essential component in turbofan engines since it drives the engine fan which produces 80 percent of the engine thrust. Therefore, overall engine performance, efficiency and fuel consumption are directly related with LPT performance and efficiency. A 1 percent increase in LPT efficiency results in fuel consumption improvements of 0.5 to 1.0 percent and overall efficiency increase of 0.7 to 0.9 [1]. LP turbines currently in service operate at efficiencies above 90 percent and increasing this efficiency through improvements in aerodynamic design gets more difficult [2]. Due to this difficulty, manufacturers look for alternative ways for reducing manufacturing and operating costs.

LPT contributes significantly not only to engine performance but also total engine weight, i.e. almost one third of the core engine [3]. Therefore, engine design improvements follow a trend towards reducing the weight of LPT stages. This involves reducing blade counts in LP turbine stages. This trend together with comparison between historical, current and future approach is illustrated in Figure 1.1.

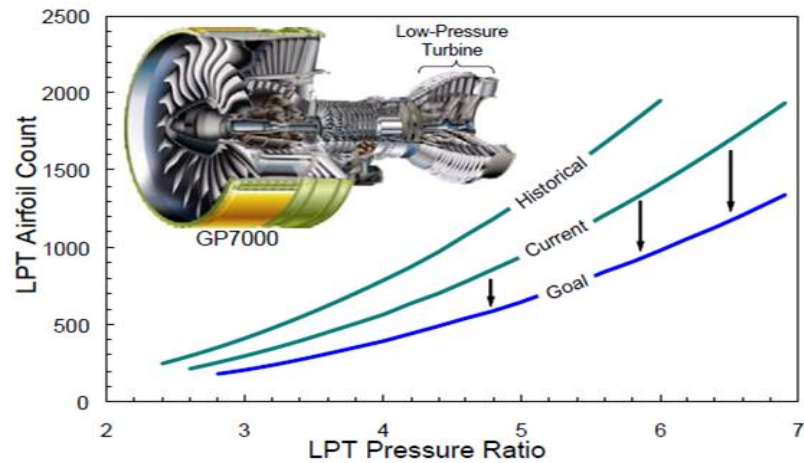


Figure 1.11: LP turbine airfoil count trend [4]

As the aim is to reduce LP turbine stage blade count without sacrificing from turbine efficiency, it will cause a significant increase in loading per blade. Highly loaded blades mean high pressure difference across the blades. That results in stronger adverse pressure gradients on the blades. In addition to that, at low Reynolds number operating conditions, i.e. at cruise altitudes, the boundary layers on LPT blades' suction surfaces are largely laminar making them prone to separation together with stronger adverse pressure gradients due to being highly loaded blades. Total pressure losses occur due to boundary layer separation and that significantly reduces the turbine efficiency. In order to successively implement highly loaded LPT blades, this loss mechanism should be eliminated or at least reduced. That is why boundary layer separation control techniques for LPT blades have long been under investigation by many researchers.

1.1 Literature Survey

1.1.1 Low Pressure Turbine Boundary Layer Separation

Laminar boundary layer separation is the primary reason for total pressure losses and therefore performance degradation of LPT blades. 300% rise in the loss coefficient due to laminar separation at low Reynolds number has been stated in the literature [6].

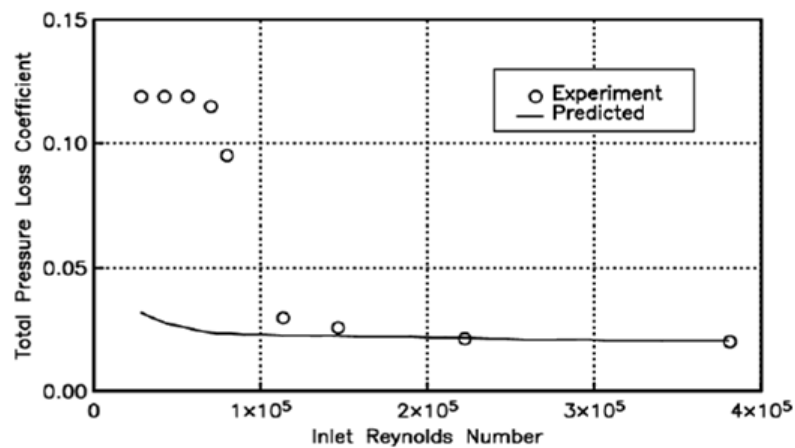


Figure 1.1.1: Total pressure losses vs. Reynolds number [5]

A laminar boundary layer on blade's suction surface separates when encountered by the strong adverse pressure gradient. The laminar separated shear layer then transitions to a turbulent shear layer and this layer reattaches to the surface, forming a closed region so called 'laminar separation bubble'. The transition occurs above the separated shear layer. The structure of the laminar separation bubble with developing transition and reattachment and the associated pressure distribution over LPT suction surface is illustrated in Figure 1.1.2.

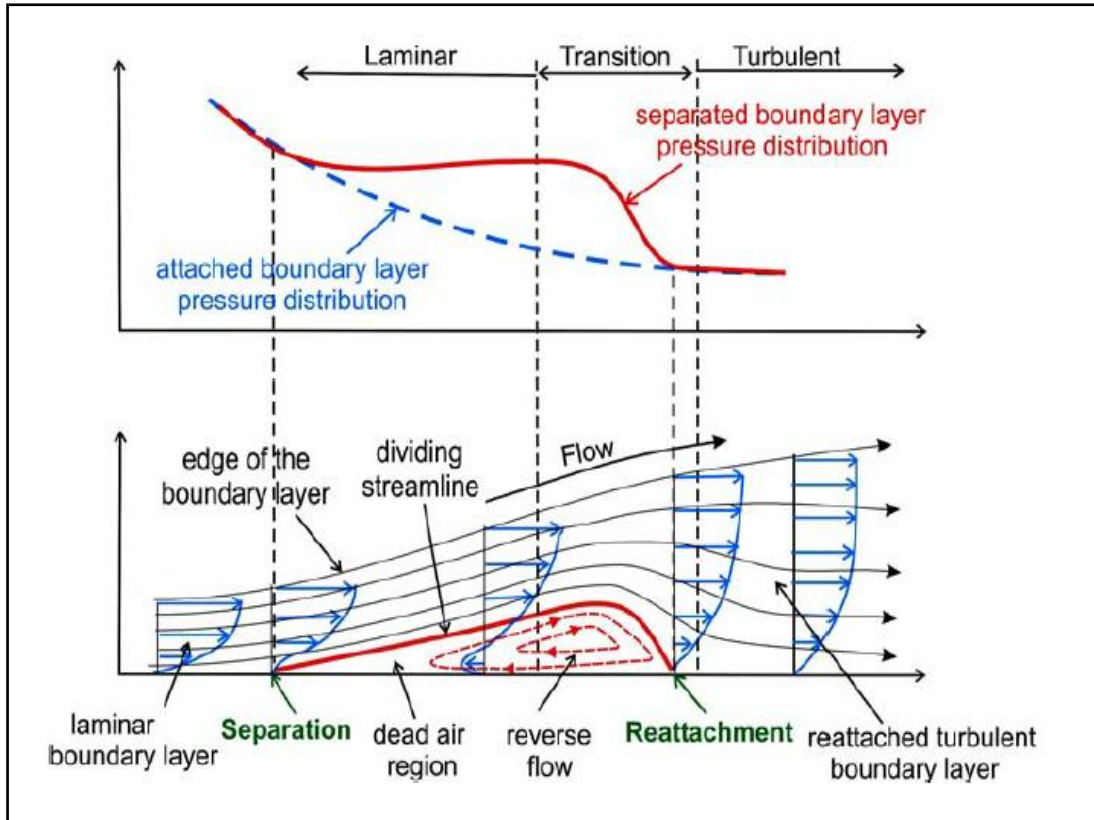


Figure 1.1.2: Schematic view of the development of laminar separated boundary layer with associated pressure distribution [3]

There is a ‘dead air’ region under the separated shear layer right after the separation point where the fluid is almost stationary and a ‘reverse flow vortex’ where the bubble exhibits the strongest momentum exchange with the freestream causing the flow to reattach [7]. Separated boundary layer pressure distribution exhibits a plateau starting from the separation point. Bubbles are classified as either short or long bubbles. This does not necessarily refer to the length of the bubble. Bubbles are considered as ‘short’ if they cause only a small deviation from the inviscid pressure distribution and as ‘long’ if they completely alter it. Long bubbles result in large profile losses and large deviations in exit flow angles in LPT blades; therefore, they should be eliminated [3].

1.1.2 Low Pressure Turbine Boundary Layer Separation Control

LPT boundary layer separation control has been the main objective of many control methods. These can be classified in two main types: passive and active control methods. Passive control methods may involve modification of the blade surface as in dimples and v-grooves or blade surface protrusions as in gurney flaps and vortex generators. While they require no additional power from the engine, they add additional drag even when control is not the aim. Volino [8] and Lake et al. [9] applied passive techniques for boundary layer separation control. They used boundary layer trip, dimples and V-grooves. They found that these passive techniques are effective in separation control at low Reynolds numbers by reducing the losses by 58%. However, these control geometries on the surface are found to result in higher losses at higher Reynolds numbers, the conditions at which the flow control is not needed. Therefore, active control methods are more favorable for their turning on and off capability when needed. Despite their cost of implementation and possible failure of control, their most remarkable feature is being able to adapt to changing flow conditions. Synthetic jets, plasma actuators and vortex generator jets are examples of active methods. The scope of this study only covers vortex generator jets (VGJs).

Vortex generator jets are created by blowing through a spanwise array of small holes. The injection is characterized by two angles: pitch and skew angles. Pitch angle (α) is formed by the jet and its projection onto the surface and the skew angle (β) is the one between the projection of the jet and the free-stream direction [10]. The schematic of the VGJ configuration is shown in

Figure 1.1.3.

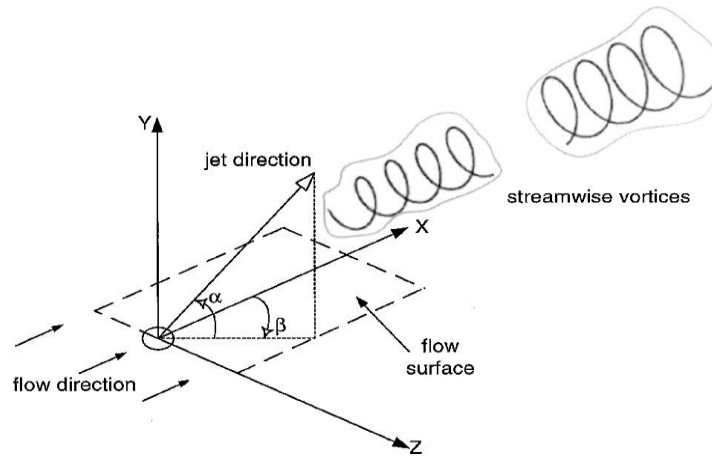


Figure 1.1.3: Schematic of VGJ, α : pitch angle, β : skew angle [11]

These angled holes are used to create streamwise vortices in a steady mode. The separating boundary layer is energized with these vortices. They bring high momentum into the near wall region promoting transition and enhancing turbulent mixing to alleviate separation [12]. This result is confirmed by Johari and Rixon [11] with the measurements for steady and pulsed jets injected into a turbulent boundary layer without a pressure gradient. Their results show that streamwise vortices created by steady jets are the dominant feature in the jet injected flow. The mechanism for the pulsed mode is rather complex and lies in the starting and ending transitions of the pulsing cycle. This experimental result is complemented by the time-accurate numerical calculations by Postl [10]. In his study, the effects of both steady and pulsed VGJs are investigated on a flat wall with streamwise pressure applied. It is shown that the mechanism responsible for reattachment for each method is different. While steady jets are found to create streamwise vortices, pulsed jets are found to introduce a two-dimensional, spanwise, unsteady wave into the flow. The effect of injection angle is also investigated and it is stated that angled (with skew angle) injection is more effective in steady mode than in pulsed mode since normal (no skew angle) injection can form spanwise vorticity which is responsible for the flow control in pulsed mode. Although recent studies are more concentrated on pulsed

VGJs for their effectiveness to eliminate separation with small amount of mass flow rates compared to steady VGJs, steady VGJs are already proved to be effective in reducing or totally eliminating boundary layer separation on LPTs. Experimental results have shown for steady VGJs to be effective over a wide range of operating conditions, i.e. Reynolds number and freestream turbulence, and control cases, i.e. implementation location and blowing ratio [13].

Johnston and Nishi [12] studied in detail the structure of steady vortex generator jets and their application on turbulent boundary layers. They were able to show that VGJs are effective in boundary layer separation control by bringing high momentum freestream to the wall. Compton and Johnston [14] identified a streamwise vortex downstream of a single jet pitched at 45° and skewed at 90° in a turbulent boundary layer. They also investigated the effectiveness of the method for various skew angles up to 180° . They concluded that the optimal skew angle producing maximum vorticity values associated with these streamwise vortices might be between 45° and 90° .

For laminar boundary layer separation control studies, specifically on LPT applications, Sondergaard et al. [13] reported a detailed study. They presented their results for a variety of steady VGJ cases: different jet blowing ratios, different jet locations and different freestream turbulence levels. It is stated that a minimum blowing ratio is essential to reduce the separation effectively. Above this value, VGJ performance does not change significantly. They determine the VGJ performance as promoting the transition in the boundary layer before separation and reducing the losses by 60%. For jet implementation location, they gave a large margin including the separation bubble and as well as 25% chord upstream of the separation point. They concluded that steady VGJ method almost eliminated the boundary layer separation and is proved to be a viable control technique. Later studies have shown that most effective location for control is around the suction peak downstream of which the separation is expected [15].

McQuilling and Jacob [16] studied both steady and pulsed VGJs on a six blade linear LPT cascade model at $Re=30,000-50,000$ using Particle Image Velocimetry (PIV) measurement technique. The results show that for a range of blowing coefficients of steady jets and reduced frequencies of pulsed jets, separation is eliminated in almost all cases. They also investigated the effect of jet location with two locations: one near leading edge, 10.5% suction surface length (SSL) and the other is 69% SSL which is just upstream of the separation point of the model blade. The location near leading edge is investigated in order to discuss the feasibility of combining separation control and film cooling techniques. However, leading edge VGJs are found not to be that effective in eliminating the separation.

Hansen and Bons [17] compared normal and angled steady jets on a flat plate before implementing on a LPT design. They used stereo-PIV so that all three velocity components were measured. Normal jets are observed to have less strength to remain closer to wall compared to angled jets which are injected at 30° pitch and 90° skew angle. This characteristic enables angled jets to promote transition better than normal jets by effectively bringing high momentum freestream closer to boundary.

1.2 Objectives and Contents of the Study

The first aim of this thesis was to work on pulsed vortex generator jets on which researchers are recently working. Due to some manufacturing problems of the model to be discussed in the following chapters, the study turned out to be a steady vortex generator jet type flow control. Although many experimental and analytical studies have been conducted in the literature on steady vortex generator jets, this study may contribute to it by presenting detailed PIV measurements. The jet configuration is also quite different from the ones in the literature. As mentioned above, this was not the aim but just an inherent outcome of the first aimed design. Independent from the method implied, the objective of this thesis is to experimentally investigate the

effects of vortex generator jet type active flow control on LPT boundary layer separation problem. The problem is presented through suction surface pressure measurements and PIV measurements. Also, the effects of the control on boundary layer separation are discussed through PIV measurements.

This thesis is presented in four chapters: Chapter 2 includes the experimental setup, procedure and measurement details. Chapter 3 discusses all the results obtained from measurements. Chapter 4 presents the conclusion, final remarks and future recommendations on the study.

CHAPTER 2

EXPERIMENTAL PROCEDURE

2.1 Experimental Setup

2.1.1 Low-Speed Cascade Wind Tunnel

The experiments are performed in a continuous-flow blower configuration wind tunnel located in the Aerospace Engineering Department at the Middle East Technical University. The wind tunnel is composed of a 0.6 m diameter double-intake radial blower driven by a frequency controlled 18.5 kW AC electric motor, a 2.6 m long rectangular to square transitional diffuser with a 7 deg diffusion angle, a 1.85 m long 1.1x1.1 m² cross-section settling chamber with multiple screens and a contraction section with an area ratio of 6.72. The tunnel has free stream turbulence intensity of 1.5 %. A fully transparent rectangular test section with 0.3x0.6 m² cross-section is placed at the exit of this transition duct. The sections of the wind tunnel together with its linear cascade test section are shown schematically in Figure 2.1.1.

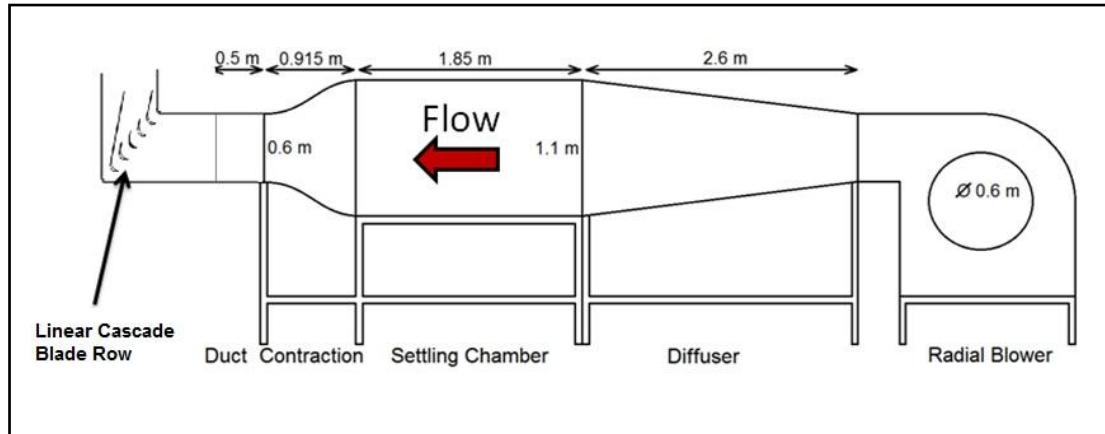


Figure 2.1.1: Sketch of Active Flow Control Wind Tunnel [18]

2.1.2 Cascade Test Section

The fully transparent test section shown in Figure 2.1.2 is made out of 0.01 m thick acrylic glass with an inlet area of $0.6 \times 0.3 \text{ m}^2$. The single blade row has T106 blade profile. T106 blade profile is a typical ultra-high loaded turbine blade with Zweifel coefficient of around 1.2 compared to conventional turbine blades which have this coefficient value of around 0.8. Five blades in the row, three fully submerged and two semi-submerged end blades, have 0.125 m axial chord. The blades are positioned such that they have zero degrees of angle of attack with respect to free stream velocity. The middle blade is the test blade and it is full span. There are two test blades, one is transparent which is used for surface pressure measurements and the other is painted black for PIV measurements. Details of the cascade are presented in Table 2.1.1.

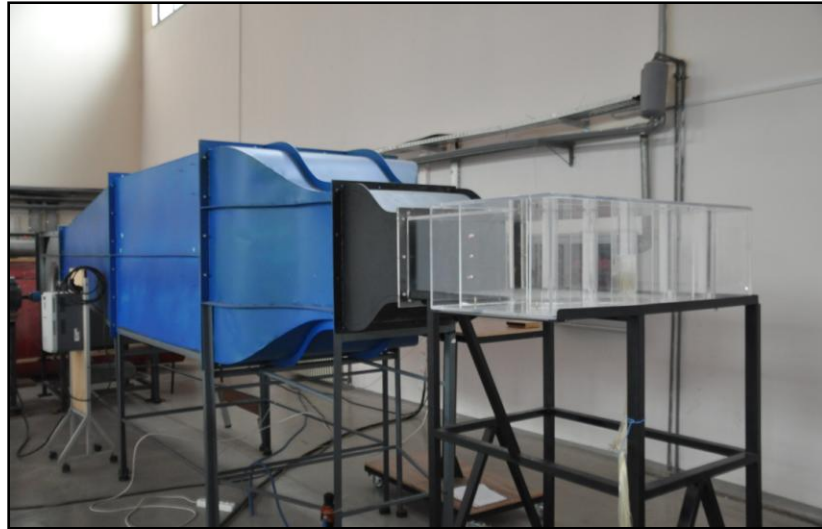


Figure 2.1.2: Fully transparent test section mounted at the exit of the contraction section

Table 2.1.1: Specifications of T106 cascade

LPT cascade test section	
Airfoil	T-106
Number of Blades	5
Axial Chord (C_x) [mm]	125
Span (b) [mm]	300
Suction surface length (SSL) (arc length from leading edge to trailing edge) [mm]	196.75
Pitch (s) to axial chord (C_x) ratio	1.024
Tip Clearance [mm]	3 (none for the test blade in the middle)
Turning Angle [deg]	99.9
Design exit flow angle, α_2 [deg]	63.2
Inlet flow angle, α_1 [deg]	37.7

2.1.3 Vortex Generator Jet (VGJ) Configuration

The mid blade, flow control integrated blade, is manufactured from ABS plastics and painted black to prevent glare from the blade surface during PIV measurements. The starting point for the control mechanism was designing a fluidic oscillator. Fluidic oscillator geometry embedded into turbine blade would serve as pulsed type vortex generator jet. The advantage would be actively controlling the flow by means of a passive geometry, i.e. pulsation just due to geometry itself without any power requirements, in contrast to solenoid valves which require additional power. The fluidic oscillator geometry chosen is the design of Huang et al. [20]. The specifications of their design can be seen in Figure 2.1.3.

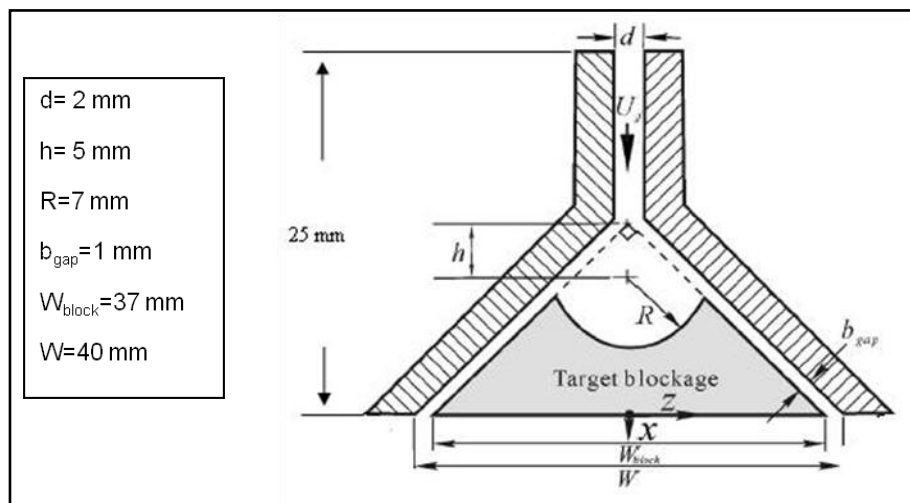


Figure 2.1.3: The fluidic oscillator geometry and its specifications [20]

A single fluidic oscillator from this design is simply manufactured from Plexiglas to be tried on a mini desktop flow visualization experiment with water jet and milk seeding and the oscillation is observed just by eye without any quantitative measurement. The observations can be seen in Figure 2.1.4.

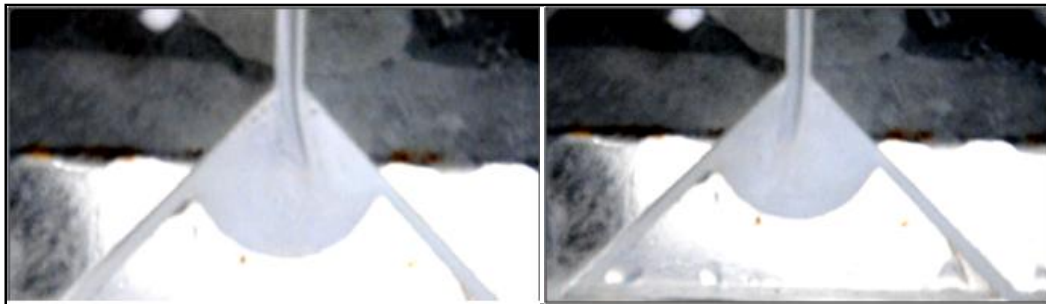


Figure 2.1.4: The consecutive snapshots of the video taken during the experiment

The flow tends to go in either direction proving the existence of an oscillating jet inside the geometry. After this preliminary experiment, this geometry is embedded inside the turbine blade. The design of the oscillator integrated blade is seen in Figure 2.1.5.

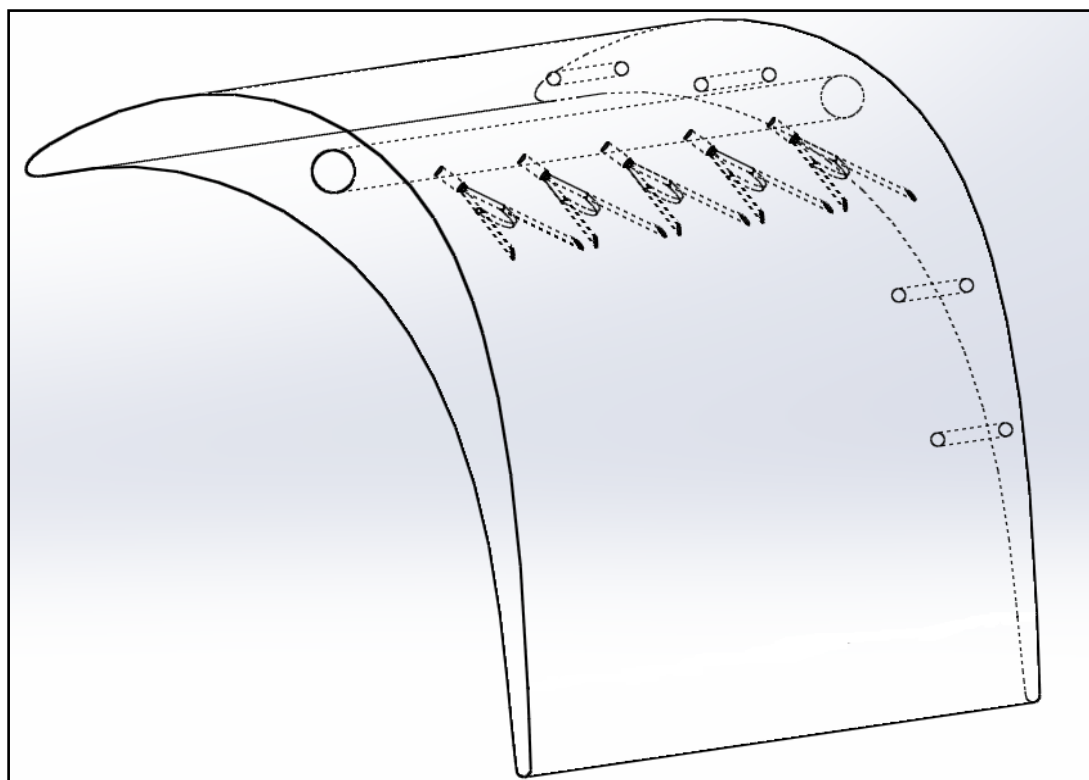


Figure 2.1.5: The solid model of the oscillator integrated test blade

This blade design needed precise manufacturing techniques. The blade had to be manufactured in two pieces and the product is seen before being glued into one piece in Figure 2.1.6.

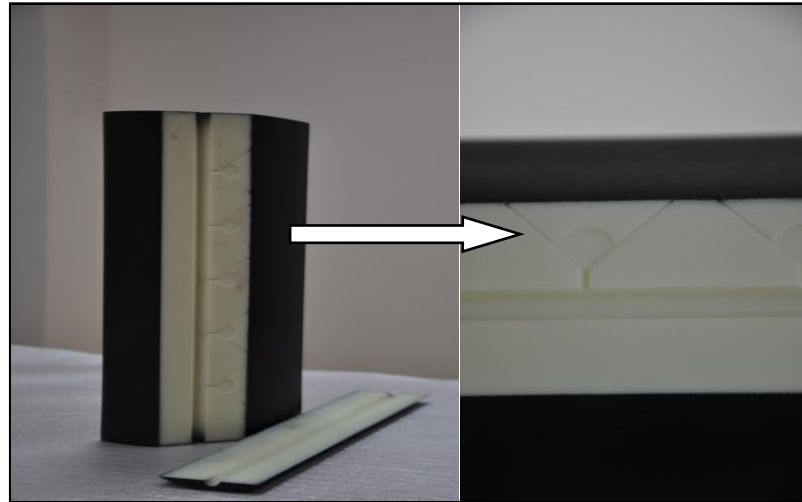


Figure 2.1.6: Fluidic oscillator integrated turbine blade in two pieces to be glued

This integrated geometry did not achieve the exit jet pulsation as expected although this geometry is already proven to be oscillating by Huang et al. [20] apart from our simple visualization experiment. This is most probably related to manufacturing because this manufacturing technique, i.e. being manufactured in two pieces, resulted in the loss of precision in the design. Being manufactured in two pieces due to manufacturing capabilities and the difficulties encountered in gluing process may be the possible reasons for the failure of periodic pulsation because the parameters in the fluidic oscillator type geometries are important and have to be achieved if oscillation is desired. Therefore, the configuration and the study to be presented turned into a steady type vortex generator jet configuration study. What remained in hand is a steady type VGJ configuration with 10 holes of 1 mm diameter (d) of five VGJ pairs each pair of which is placed $10d$ apart. Typically, the spanwise spacing of the jet holes is $10d$ or greater in separation control applications [21]. The jets are injected into the flow at a pitch angle of 30 deg and a skew angle of 45 deg

inherently due to the fluidic oscillator geometry embedded. This configuration, although set by fluidic oscillator geometry, is consistent with a typical VGJ configuration which is usually seen to have low pitch angle (30-45 deg) and aggressive skew angle (45-90 deg). The holes are located at 50% SSL considering the suction peak location of the blade (44% SSL). This is based on the fact that the separation control is effective when the holes are placed around the suction peak downstream of which the separation is expected [15]. The jet holes are fed from both ends of the blade through a spanwise drilled plenum of 8 mm diameter shown in the solid model of the blade (Figure 2.1.5). Two pressure regulators are connected between the air plenum and the compressor.

2.2 Measurement Details

2.2.1 Surface Pressure Measurements

The mid blade is instrumented with conventional static pressure tappings for steady surface pressure measurements. These taps are drilled 1.5 mm in diameter normal to blade surface at the mid span in the chordwise direction and have l/d ratio of 2, where l is the hole length and d is the hole diameter, except for the last two holes which have 1.33 due to thickness limitation of the blade. The l/d ratio is chosen accordingly to ensure that errors in pressure readings are independent from that ratio [19]. Measurements are done by a Scanivalve DSA-3217 16 channel pressure scanner. Half of the 16 channels have 0.5 psi pressure range and the rest has 1 psi. Brass tubes of the same inner diameter of taps are connected to the exit of taps and then through PVC tubing they are connected to channels. Suction surface has 20 and pressure surface has 16 pressure taps. Four wind tunnel runs are needed to take 36 tap measurements from 16 channels provided that 9 channels are kept at the same tap

in each run to ensure the repeatability of the experiments. The pressure tapped blade can be seen in Figure 2.2.1. The tap locations are presented in Table 2.2.1.

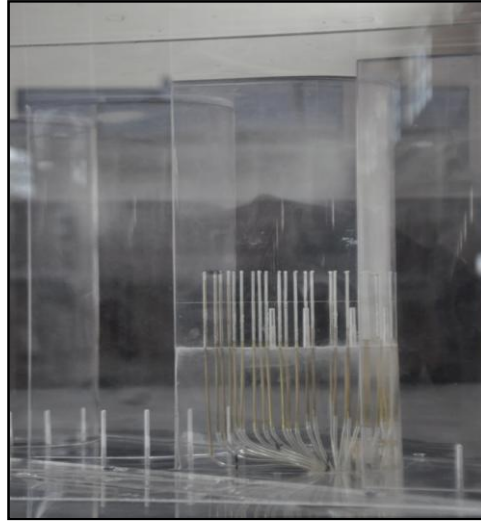


Figure 2.2.1: Pressure tapped blade

Table 2.2.1: Pressure tap locations

Tap no. Upper(U)	U1	U2	U3	U4	U5	U6	U7	U8	U9	U10
s/SSL (%)	0.03	0.05	0.08	0.10	0.15	0.20	0.26	0.32	0.37	0.42
Tap no.	U11	U12	U13	U14	U15	U16	U17	U18	U19	U20
s/SSL (%)	0.44	0.50	0.57	0.62	0.67	0.71	0.75	0.81	0.85	0.90
Tap no. Lower(L)	L1	L2	L3	L4	L5	L6	L7	L8	L9	L10
s/SSL (%)	0.03	0.06	0.075	0.1	0.15	0.2	0.26	0.32	0.4	0.46
Tap no.	L11	L12	L13	L14	L15	L16				
s/SSL (%)	0.5	0.55	0.62	0.71	0.75	0.77				

The static pressure coefficient, C_p , is calculated as:

$$C_p = \frac{P_{01} - P_s}{P_{01} - P_{2s}} \quad (\text{Eqn. 2.1})$$

where P_{01} is the cascade inlet total pressure, P_{2s} is the exit static pressure measured at $0.5C_x$ downstream of the blade trailing edge, and P_s is the measured static pressure. This definition of C_p can also be called as the ratio of inlet dynamic head to isentropic dynamic head. This definition is chosen in order to be compatible with the work of Zhang [3] who has also worked on separation problem on the same T106 blade profile except for pitch-to-chord ratio.

2.2.2 Total Pressure Measurements

Measurements are performed at $0.5C_x$ downstream of the blade row at midspan on a pitchwise line using a Kiel probe with a shield diameter of 3.175 mm. Data are acquired using Scanivalve DSA-3217 16 channel pressure scanner described in the previous sub-heading. The probe is traversed along pitchwise direction using a Velmex traverse mechanism which has a displacement resolution of 0.00635 mm. The schematic of the measurement plane is shown in Figure 2.2.2.

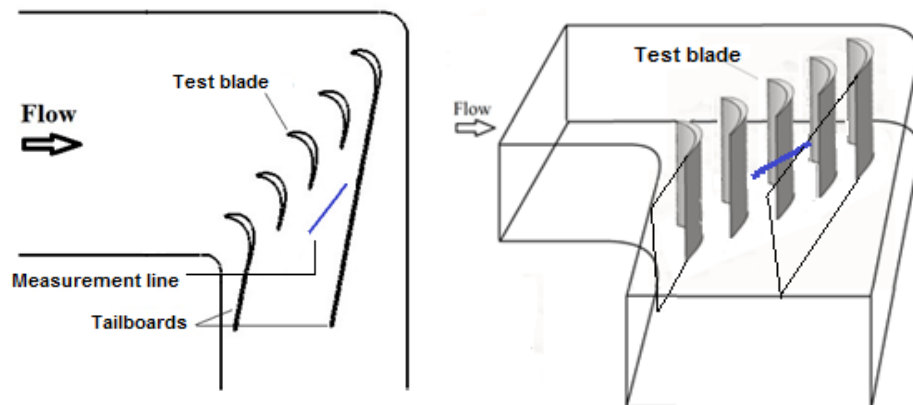


Figure 2.2.2: Total pressure measurement line, top view (left), 3-D view (right)

Total pressure loss coefficient is defined as:

$$C_{p,loss} = \frac{P_l - P_{01}}{0.5\rho U_\infty^2} \quad (\text{Eqn. 2.2})$$

where P_l is the measured local total pressure, P_{01} is the cascade inlet total pressure and U_∞ is the free stream inlet velocity.

2.2.3 2D Particle Image Velocimetry (PIV) Measurements

A TSI Particle Image Velocimetry (PIV) system is used for 2-D boundary layer measurements. The system consists of 30 mJ/pulse Nd:YLF high-speed laser and a 12-bit high-speed Phantom camera that has the capability to operate individually at 1.5 kHz at a 4 megapixel resolution. A 105mm Macro Sigma lens is used with an aperture setting of f#2.8. Additionally, 20 mm extension tube is used to be able to increase the magnification. The camera is operated at 742 Hz with 4 megapixel resolution which is the maximum resolution achieved when the camera is synchronized with the laser. The camera is precisely traversed between different windows using the TSI Isel Traverse System. The flow is seeded with a commercial fog generator which uses a fog liquid of glycol mixed with water. A picture of the experimental setup for PIV measurements can be seen in Figure 2.2.3 (a) and a simple sketch of the tunnel test section with the laser sheet is shown in Figure 2.2.3 (b).

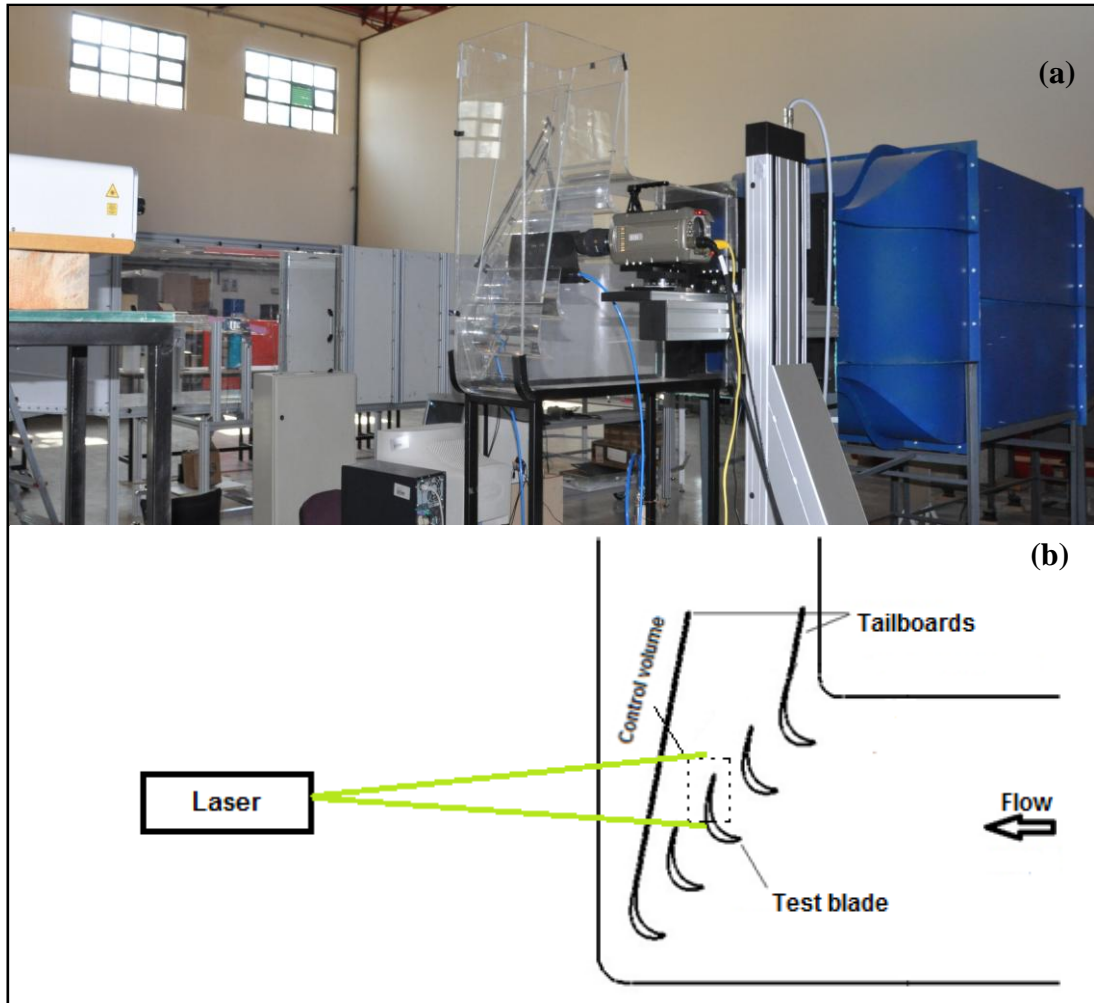


Figure 2.2.3: (a) PIV experimental setup (b) sketch of the test section with laser sheet

PIV measurements are performed within a field of view of $24 \times 38.5 \text{ mm}^2$. The measurements are performed at three different spanwise locations. One is mid-span ($z/d=0$) which corresponds to midpitch of one pair of VGJ holes, the other is aligned between two adjacent counter-rotating VGJ holes ($z/d=25$) and the last is midway between these two planes ($z/d=12.5$). The sketch of measurement planes can be seen in Figure 2.2.4.

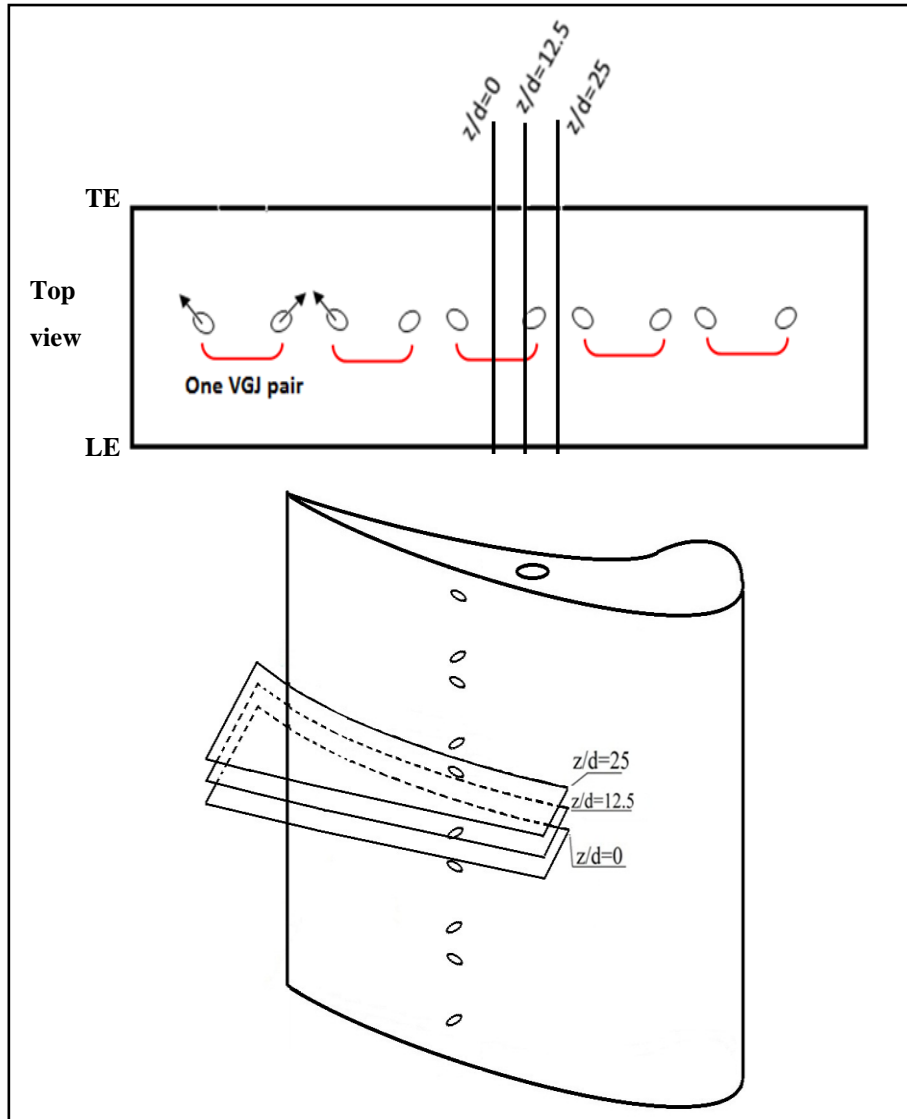


Figure 2.2.4: Sketch of measurement planes, LE: Leading Edge, TE: Trailing Edge

Sketch of one representative PIV measurement plane and measurement windows are given in Figure 2.2.5.

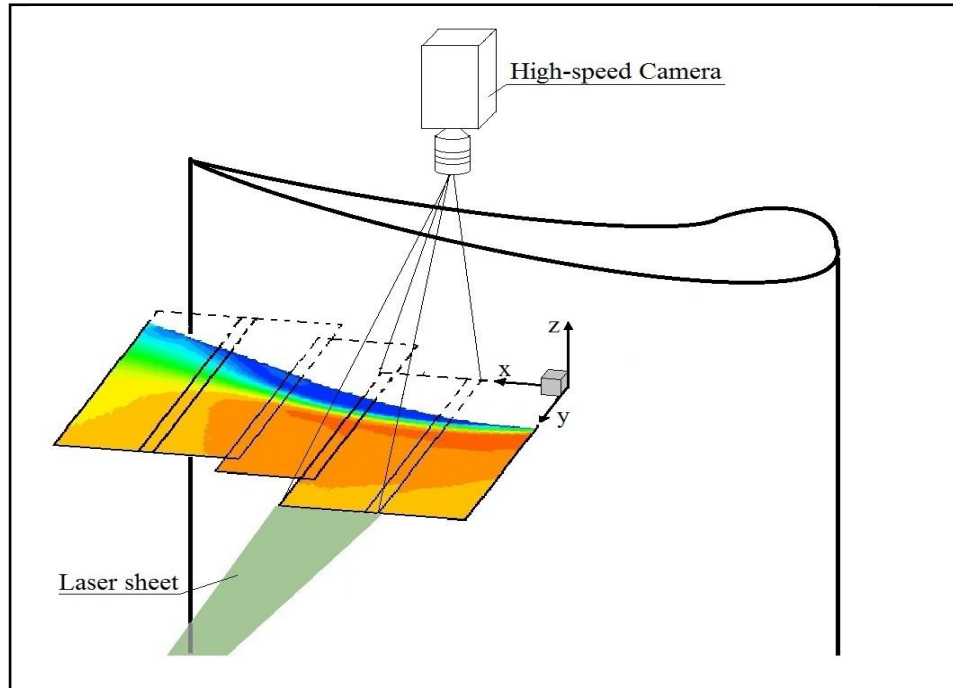


Figure 2.2.5: Sketch of PIV measurement plane and windows

The time difference between the two laser pulses (Δt) for no flow control case at midspan ($z/d=0$) is $12 \mu\text{s}$ which is adjusted based on the principle of obtaining a detectable pixel displacement between the two successive images. This value is reduced with the jet injection to $3 \mu\text{s}$ for the measurements at $z/d=25$. Images of five overlapping (10% overlap) windows are taken to cover the suction surface of the blade after around 55% suction surface length (SSL). These windows are reduced to four for injection cases. On each measurement plane, for each injection scenario, 450 image pairs are obtained. The vector maps are obtained using TSI Insight 4G software. Background subtraction is used as pre-processing algorithm to be able to remove the background noise from the images. An adaptive algorithm with 64×64 pixels starting spot dimensions and going down to 32×32 pixels with 50% interrogation area overlap is used for processing scheme. The vector spacing obtained with this interrogation area is around 0.5 mm. Post-processing algorithms are beneficial if bad vectors still exist after processing. It is based on locally

validating the vector maps by using local median and vector conditioning by filling the holes in vector field using local mean.

450 instantaneous data are ensemble-averaged to obtain the average vector field. All measurement data are taken at $Re=29000$ (based on cascade inlet velocity and axial chord) which is consistent with LPT separation problem studies, stated to be representative of cruise conditions of turbofan engines [25]. The temperature of the flow is almost constant at $23\text{ }^{\circ}\text{C}$ so that Reynolds number can be said to be not changing throughout the experiment.

2.2.4 Injection Scenarios

Injection scenarios are set by available equipments in the laboratory. The jet exit velocities are measured using a total pressure measurement instrument, namely Kiel probe, assuming atmospheric pressure as static pressure. In addition, the jet exit velocities are assumed to be uniform through each hole. Three steady blowing cases are selected and they are characterized according to the following definition:

Blowing ratio:
$$B = \frac{U_j}{U_{\infty}} \quad (\text{Eqn. 2.3})$$

where U_{∞} is the inlet freestream velocity at a value of 3.5 m/s and U_j is the mean jet velocity.

The description of the jet injection is sketched in Figure 2.2.6 and the steady blowing cases are given in Table 2.2.2 by the blowing ratio parameter:

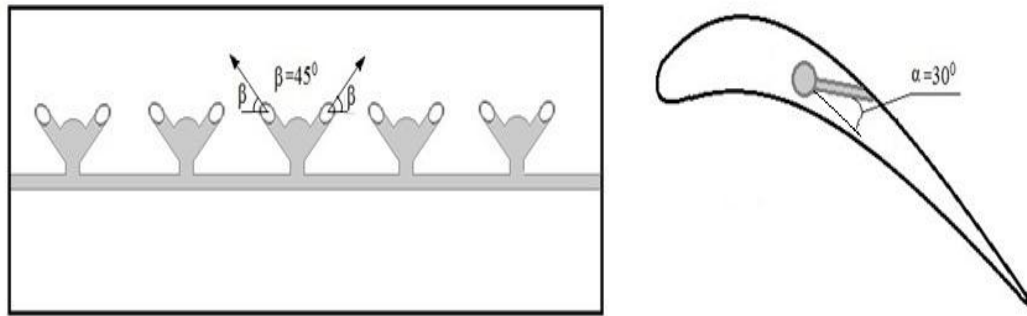


Figure 2.2.6: Description of the jet injection

Table 2.2.2: Steady blowing cases

Case	B
1	2.2
2	4.4
3	7.2

Only $z/d=0$ measurement plane involves all cases. At $z/d=12.5$ and $z/d=25$ planes, only the first two cases are examined.

2.2.5 Uncertainty Estimates

The variation in the test section inlet velocity during the experiments is less than 1% [22]. The instrument for surface pressure measurements, namely Scanivalve DSA 3217 pressure scanner, has an accuracy of 0.12%. Therefore, the uncertainty estimate of surface pressure measurements is said to be in that range. The error due to temporal variations in the laser pulse synchronization is negligible. The displacement accuracy of the TSI Isel Traverse System is $\pm 300 \mu\text{m}$. As to the statistical error due to using 450 vector maps for averaging, Uzol et al. [23] quantified the convergence errors due to using 100 vector maps compared to using 1000 vector maps in a

turbulent rotor wake of an axial turbomachine. Maximum observed errors in mean velocities and the turbulent kinetic energy was around 5% and 8%, respectively. Therefore in this study statistical convergence errors are expected to be less than those levels. The spatial displacement accuracy of the PIV's cross-correlation algorithm is less than approximately 0.1 pixels. This is expected to generate a spatial displacement error on the order of less than 2% for a particle displacement of about 5 pixels [24], which are typical displacements in this study.

CHAPTER 3

EXPERIMENTAL RESULTS AND DISCUSSION

3.1 Baseline Case ($B=0$)

No blowing baseline case is presented in order to understand the extent of the laminar separation bubble problem on T106 LPT blade under operating conditions specified. Only after this investigation can one understand the effects of VGJ application on the separation problem.

To be able to decide on operating conditions, experiments are performed at different inlet free stream velocities. The decision was made on the basis of resolving the flow structure inside the bubble as a result of PIV measurements. The more severe the separation, the thicker the laminar separation bubble is; therefore, the phenomena related to bubble dynamics are easily observed during experiments. Two cases are discussed here, namely $Re=29000$ and $Re=58000$. Both cases are in the range of a typical turbofan engine cruise conditions [25]. Figure 3.1.1 gives the comparison between $Re=29000$ and $Re=58000$ for non-dimensional mean inplane velocity contour plots.

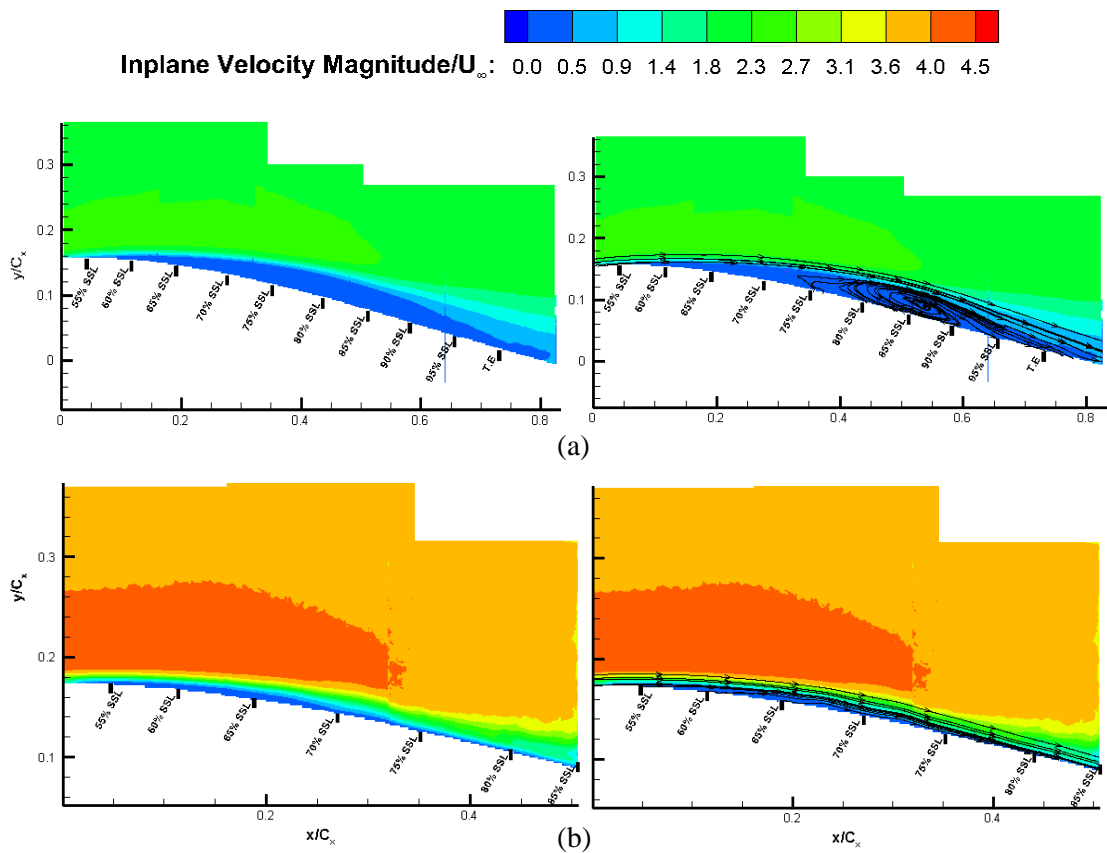


Figure 3.1.1: In-plane velocity magnitude/ U_∞ contours for (a) $Re=29k$ (b) $Re=58k$, $B=0$

The interpretation of the plots will be given in more detail in the following discussions; however, the figure clearly shows that lower Re case allows resolving the flow structure inside the bubble better than higher Re does. This is evident by the streamlines drawn on the contour plots. In addition, the bubble zone, which can be detected by blue contours of low velocity values on the plots, is thicker and more observable at low Re case. For this thick separated zone, the flow control effectiveness is believed to be more obvious when applied. Therefore, $Re=29000$ case is chosen as the operating condition for this study.

3.1.1 Surface Pressure Measurement Results

Mid-span surface pressure measurements are performed on the pressure tapped T106 blade details of which are given in Chapter 2. The time-averaged C_p distributions at $Re=29000$ are shown in Figure 3.1.2. Both suction and pressure surface results are presented for a steady inflow.

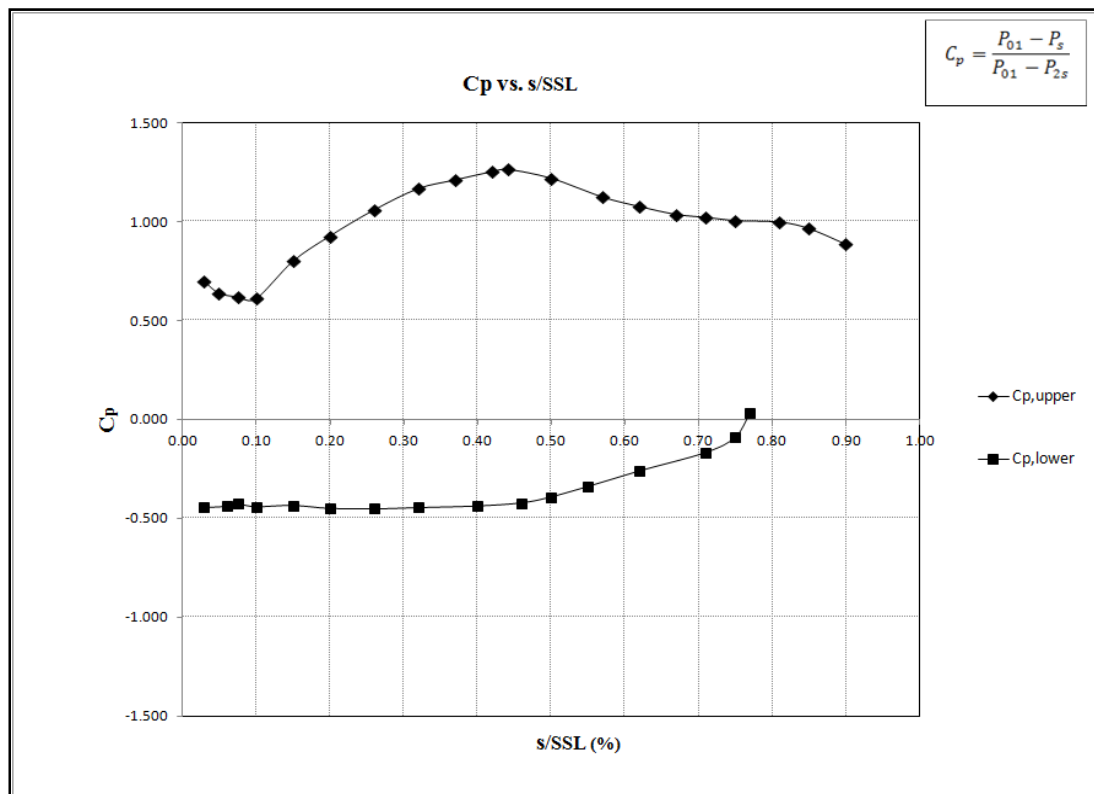


Figure 3.1.2: Surface C_p distribution. $Re=29k$, $B=0$

Peak suction can be inferred from the plot with the guidance of tap locations as $s/SSL=0.44$. Referring to a typical C_p distribution with laminar separation bubble (Figure 1.1.2), it can be said that there is a laminar separation and corresponding bubble over the rear portion of the blade with separation starting between $s/SSL=0.55$ and $s/SSL=0.60$. Low Re conditions result in large separation bubbles extending over a larger portion on suction surface since reattachment point moves further aft on the

blade under these conditions. Reattachment point cannot be seen in this plot since there is no pressure tap located after $s/SSL=0.90$, the locations very near to trailing edge, due to blade thickness constraints. However, the existence of reattachment can be inferred from recovery of the pressure plateau, typically associated with the separated shear layer, after around $s/SSL=0.85$ and which is later to be proved by PIV results. Suction peak and separation location are in accordance with T106 studies in literature ([3], [26]).

3.1.2 2D Particle Image Velocimetry Measurement Results

Velocity and Turbulence Field Results

Under the same operating conditions with C_p measurement, 2D PIV measurements are performed for the baseline case at blade mid-span ($z/d=0$). Contour plots presenting these measurement results are given from Figure 3.1.3 to Figure 3.1.6.

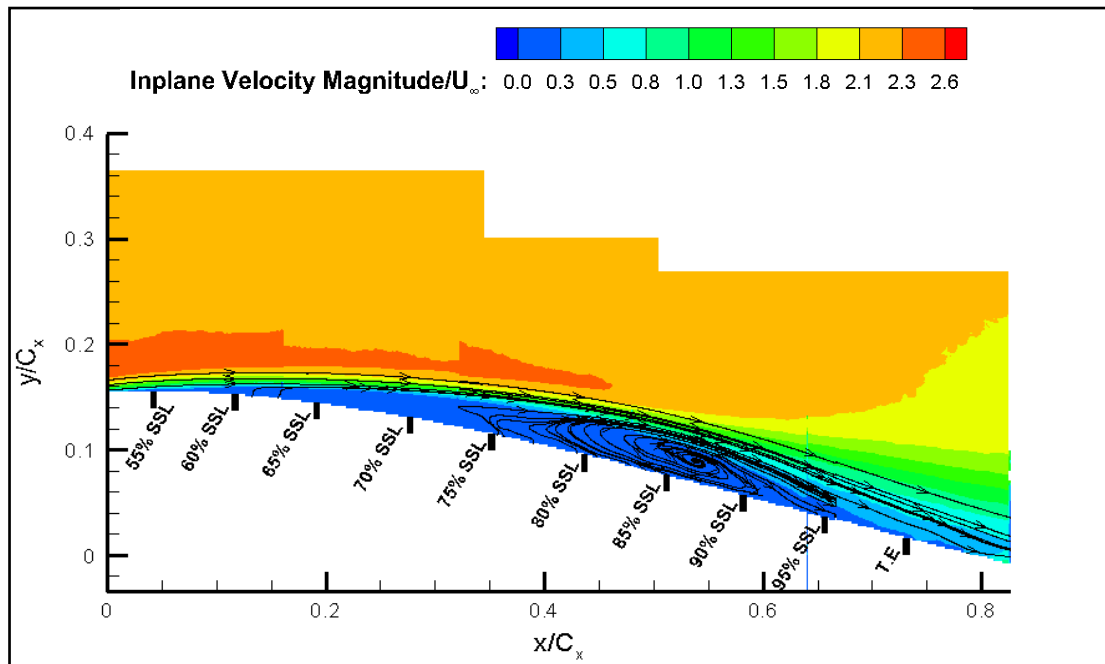


Figure 3.1.3: In-plane mean velocity magnitude/ U_∞ contours at $z/d=0$ showing the aft portion of the blade (55% SSL-Trailing Edge (TE)). The flow is from left to right, $B=0$ and $Re=29k$

In Figure 3.1.3, the separation is observed with a boundary layer thickening starting from after 55% SSL and extending until the point of reattachment which is around 95% SSL. This closed region is called laminar separation bubble. The laminar-to-turbulent transition occurs over the bubble. The most remarkable characteristic of a laminar separation bubble can be seen in this figure with a recirculation zone and vortical structure formation at around 85% SSL illustrated by streamlines. This recirculation zone creates vortical motion where the streamlines are closed; therefore, it is called reverse flow vortex. This reverse flow vortex occurs before the reattachment point and involves the strongest momentum exchange with the free stream causing the flow to reattach. After reattachment point, the flow is already transitioned to turbulent. In Figure 3.1.4, turbulent kinetic energy levels are low when the flow separated as a laminar flow. Once the transition to turbulence starts, high turbulent kinetic energy levels are depicted in the figure. The highest levels of the TKE can be attributed to bursting of turbulent spots in the transition region. Since

the flow reattaches as turbulent, turbulent kinetic energy levels are still in reasonable levels. One point is worth to mention here that the transition seems to occur near the boundary after some point; it starts over the separated shear layer but near the reattachment point, the entrained fluid particles are brought to boundary evident by high levels of TKE. That is, the final transition seems to be occurring close to boundary indicating that laminar separation bubble is partially laminar.

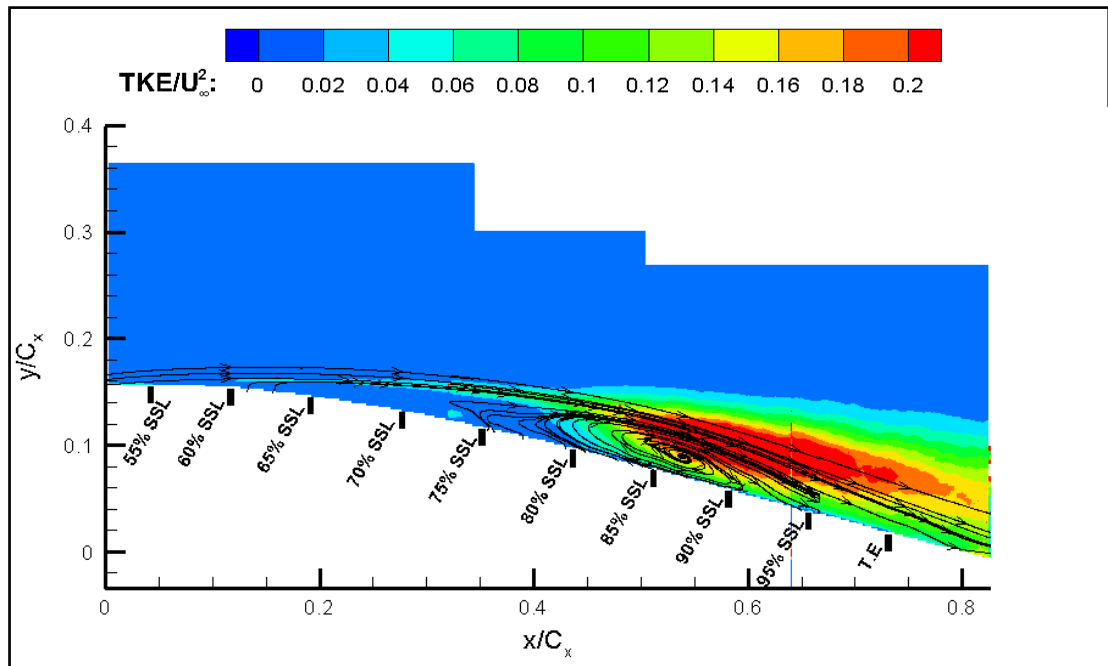


Figure 3.1.4: Turbulent kinetic energy/ U_{∞}^2 contours at $z/d=0$ showing the aft portion of the blade (55% SSL-Trailing Edge (TE)). The flow is from left to right, $B=0$ and $Re=29k$

Vorticity contours also figure out the separation and transition to turbulence locations. As can be seen in Figure 3.1.5, inside the boundary layer, before the separation occurs, the vorticity is produced and is negative as expected since $\frac{\partial U}{\partial y}$ is positive inside the boundary layer. Outside the boundary layer, vorticity is zero. This is attributed to the fact that in boundary layer theory, the external flow is assumed to be irrotational. Once the boundary layer separated, under the separated shear layer,

vorticity is zero; this region belongs to bubble's 'dead air region' in which the fluid is almost stationary [7]. Over the region around 85% SSL, laminar-to-turbulent transition results in vorticity production in a larger area. Decaying of vorticity after reattachment point is related to convection of vortices shed from laminar-to-turbulent transition.

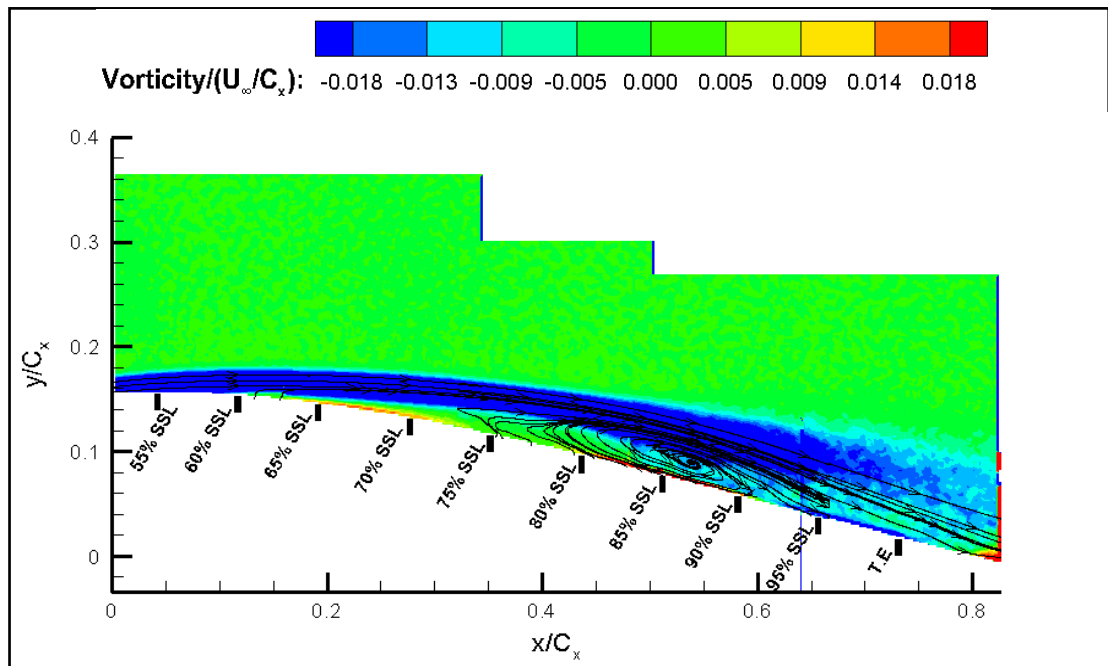


Figure 3.1.5: Non-dimensional mean vorticity, $\Omega_z / (U_\infty / C_x)$, contours at $z/d=0$ showing the aft portion of the blade (55% SSL-Trailing Edge (TE)). The flow is from left to right, $B=0$ and $Re=29k$

As for the Reynolds shear stress per unit mass, $-\overline{u'v'}$, in Figure 3.1.6, it can be said that until the middle of the separation bubble Reynolds shear stress remains at low levels around almost zero. It increases with the starting of the transition because Reynolds shear stress is related to dynamics of vortical structures which are the vortices shed during the momentum exchange of the boundary layer with the free-stream flow prior to reattachment. The reattachment point and the downstream of it are the regions where Reynolds shear stresses are dominant. This can be attributed to

the fact that the flow reattaches as turbulent because Reynolds shear stresses are dominant in a turbulent boundary layer.

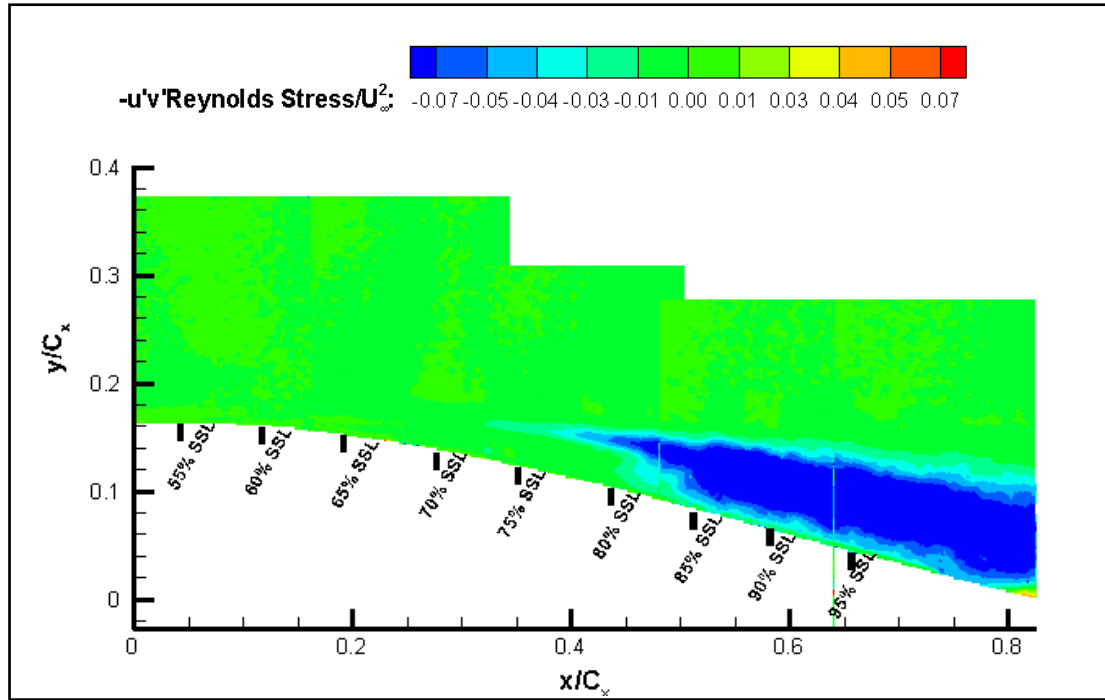


Figure 3.1.6: $-\overline{u'v'}/U_\infty^2$ contours at $z/d=0$ showing the aft portion of the blade (55% SSL-Trailing Edge (TE)). The flow is from left to right, $B=0$ and $Re=29k$

Although the shedding frequency of the vortices created during transition is not measured in this study, relying on the high values of the frame rate of the PIV camera, instantaneous contour plots can also be presented in case vortex dynamics can be captured. Instantaneous velocity magnitude and vorticity contour plots are presented in Figure 3.1.7 and Figure 3.1.8, respectively, for five windows encompassing from 55% SSL to TE of the blade surface. The three images in one row are the consecutive images separated just by dt set by the camera frame rate which is $1/742$ (~ 0.00135) seconds in our case.

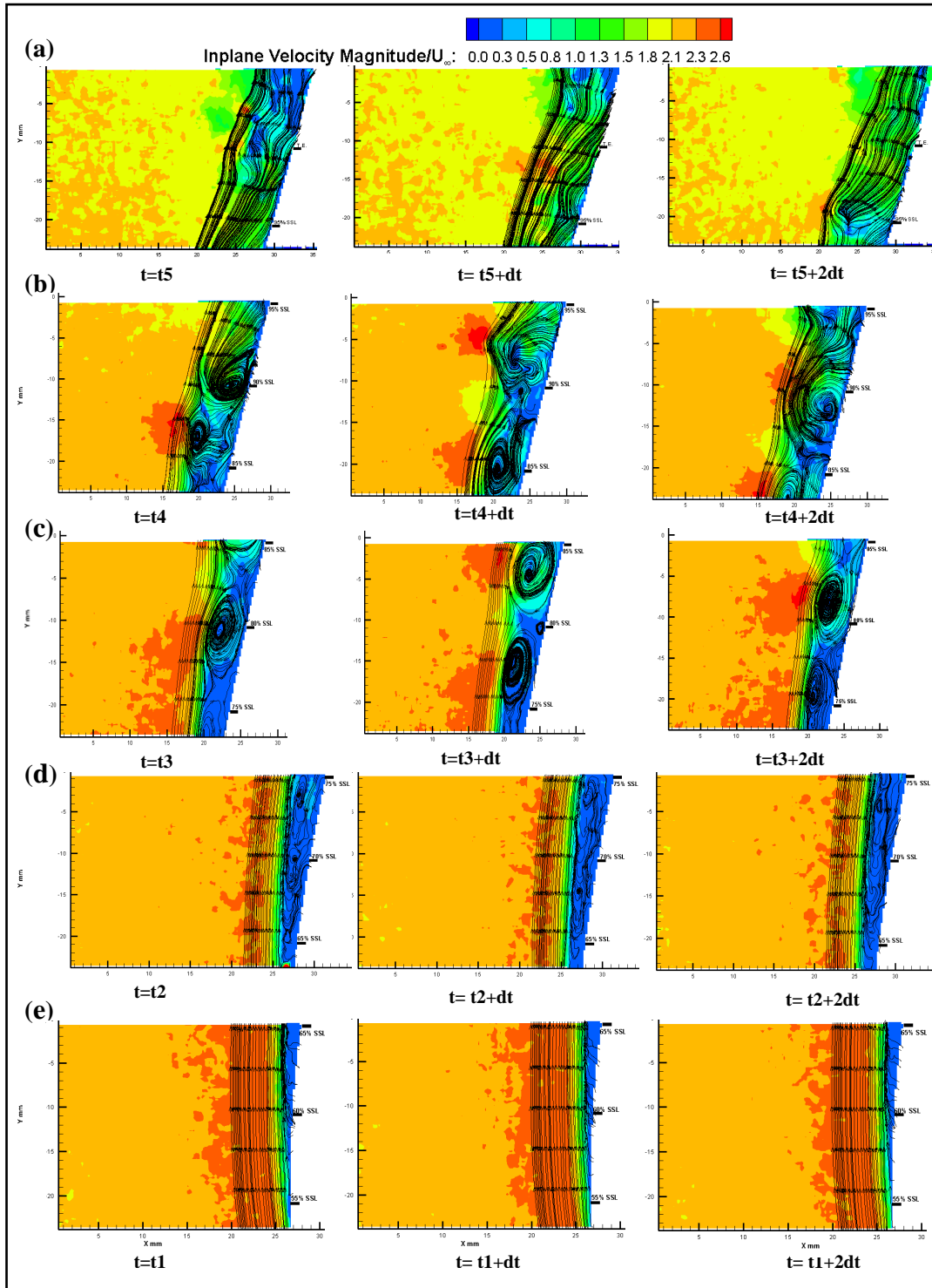


Figure 3.1.7: Instantaneous in-plane velocity magnitude/ U_∞ contours at $z/d=0$ showing the regions (a) 95% SSL- TE (b) 85% SSL-95% SSL (c) 75% SSL- 85% SSL (d) 65% SSL-75% SSL (e) 55% SSL- 65% SSL. The flow is from bottom to top, $B=0$ and $Re=29k$

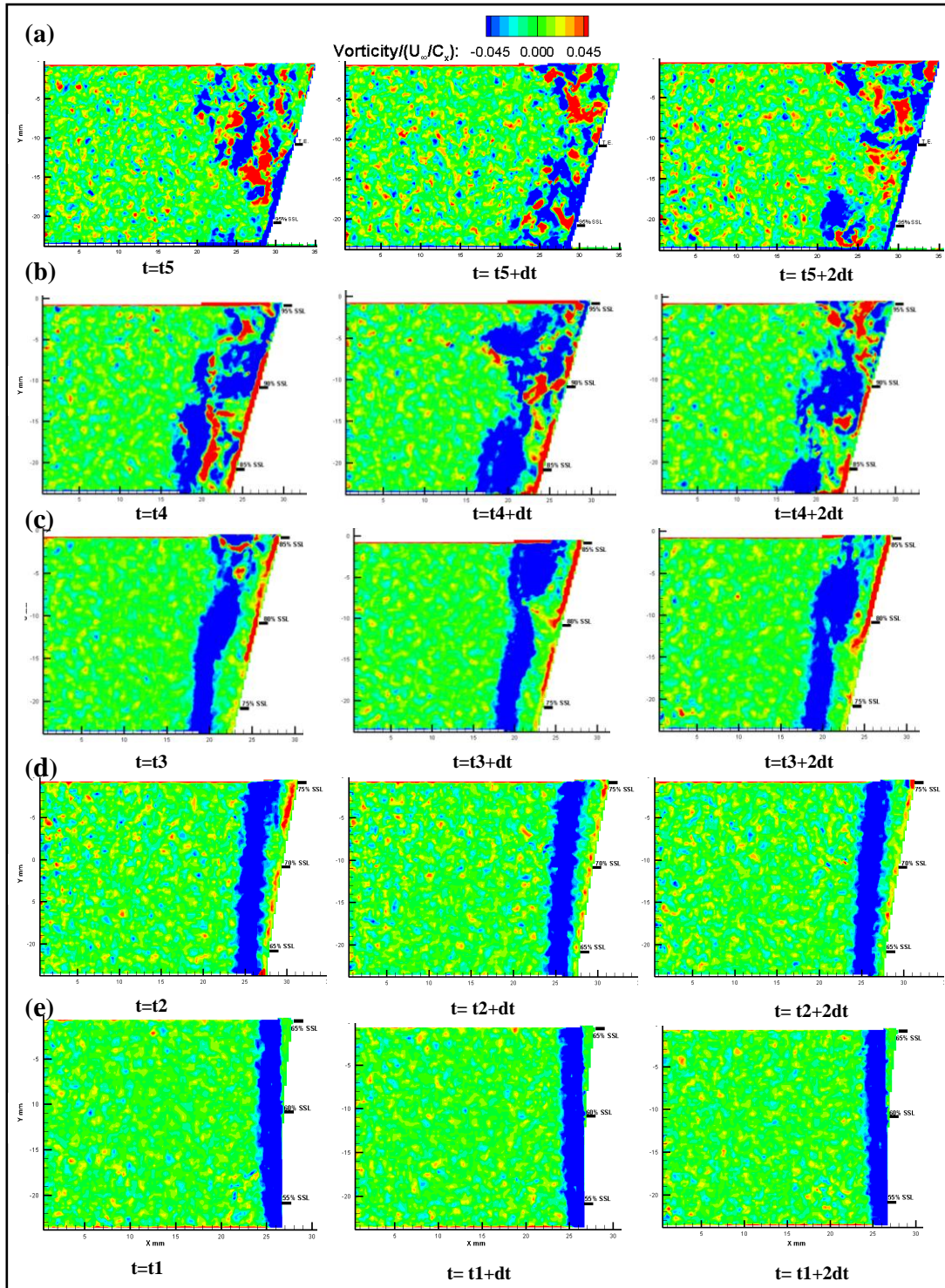


Figure 3.1.8: Instantaneous vorticity (Ω_z)/(U_∞/C_x) contours at $z/d=0$ showing the regions (a) 95% SSL- TE (b) 85% SSL-95% SSL (c) 75% SSL- 85% SSL (d) 65% SSL-75% SSL (e) 55% SSL- 65% SSL. The flow is from bottom to top, $B=0$ and $Re=29k$

From Figure 3.1.7, it can be detected that vortical motion starts from third window (c) and gets bigger in the following window as evident by the streamlines. The separation zone is thicker in (b) than the one in (c) since fourth window (b) is closer to reattachment point, even involves it at 95% SSL. Also from Figure 3.1.7, vortex movement can be detected in three consecutive images separated by small time differences; but still we are not sure that it is the shedding of the vortices due to lack of shedding frequency information. In (b), the movement of vortices are more detectable since this window involves the reattachment point before which the reverse flow vortex is the strongest. The fifth window involves the convection of vortices in the wake of the blade which are created during transition since this window encompasses a small region after TE of the blade. From Figure 3.1.8 (c), the movement of the vortices are obvious over the separated shear layer whereas this movement is brought closer to wall in (b) due to the high levels of entrainment between the boundary layer and freestream before reattachment.

Boundary Layer Analysis

Apart from contour plots, the velocity profiles along the boundary will be more helpful to identify the separation, transition and reattachment locations. To be able to obtain the profiles, points normal to blade surface are determined at specified stations along the blade surface. The points to be extracted are determined as the points on the line normal to local tangent of the blade surface at specified station. Mean flow quantities of these points are extracted. These quantities are in measurement coordinate, i.e. x-y coordinate, although it should be in local blade coordinate, i.e. s-n. To do that, transformation matrix is used to transform the quantities in x-y coordinate to s-n coordinate using the transformation relation $[A'] = [R]^T[A][R]$ where $[A]$ is the matrix to be rotated by the rotation matrix $[R]$ to form the rotated matrix as $[A']$. $[A]$ can be either vector or 2-D tensor. The rotation matrix is written in the following form.

$$[R] = \begin{bmatrix} \cos\theta & \sin\theta \\ -\sin\theta & \cos\theta \end{bmatrix}$$

where θ is the counterclockwise angle between the coordinate system and the new coordinate system. All these coordinate systems mentioned and specified stations are sketched in Figure 3.1.9.

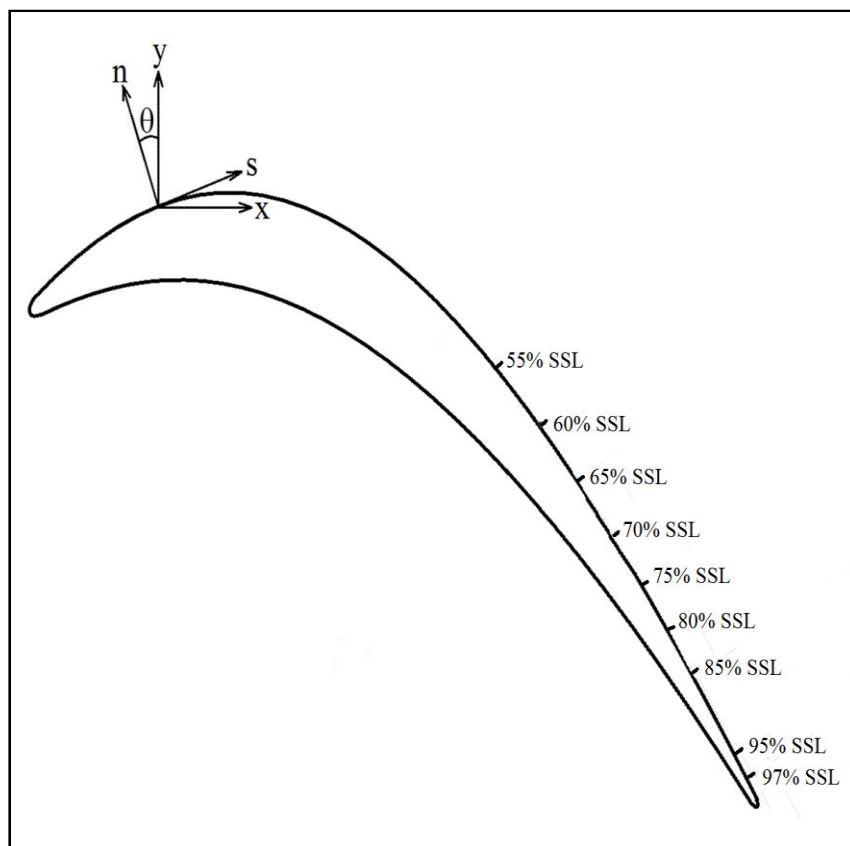


Figure 3.1.9: Coordinate systems and specified SSL stations

Figure 3.1.10 presents the development of the boundary layer with velocity profiles at specified s /SSL stations.

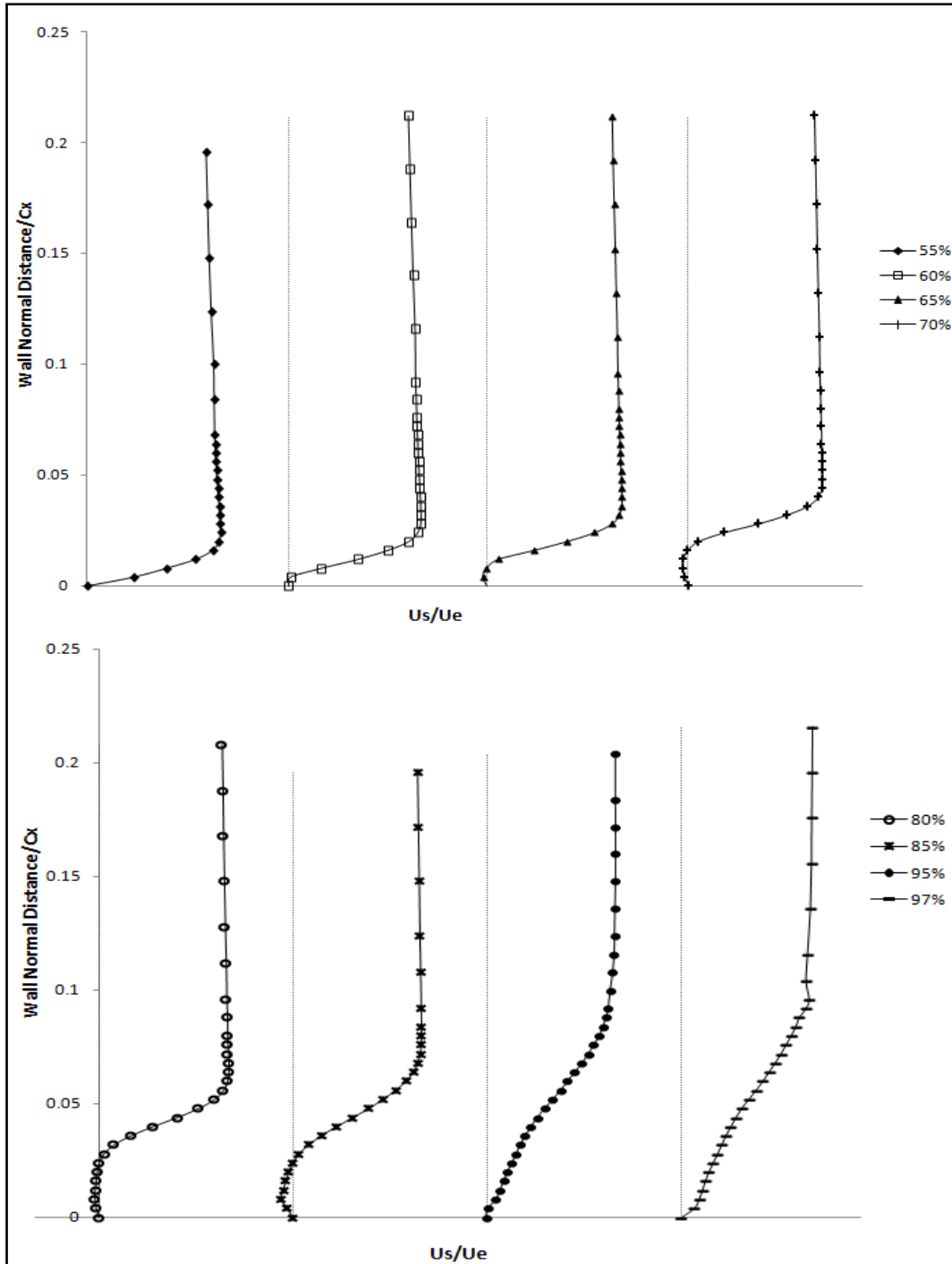


Figure 3.1.10: Boundary layer profiles of mean streamwise velocity normalized by local edge velocity; profiles at different s/SSL stations at $z/d=0$, $B=0$, $Re=29k$.

The velocity values are normalized by the local edge velocity at that station to be able to obtain the profiles as correctly as possible. It can be seen from Figure 3.1.10 that at 55% SSL, the velocity profile indicates an attached flow. The inflection point develops at 60% SSL station indicating a clear separation. The stations after 60% SSL are inside the laminar separation bubble clearly seen by the velocity profiles indicating a reverse flow region with negative velocity values. Being consistent with the streamlined velocity magnitude contour plots, velocity profile at 85% SSL is indicative of the transition region before reattachment where the velocity profiles have the strongest reverse flow percentages. By 95% SSL, the boundary layer has reattached as turbulent and a turbulent boundary layer is being developed. This development can be seen in the recovery of the velocity profiles after reattachment, namely at 97% SSL.

Separation line can be drawn starting from the separation point and passing through all inflection points of the velocity profiles of the stations inside the adverse pressure gradient zone and finally closing down at the reattachment point. The height of the laminar separation bubble can be estimated using the relation between the ordinate value of separation line and ordinate value of the bubble suggested by van Ingen and Boermans [27] and presented as in Figure 3.1.11.

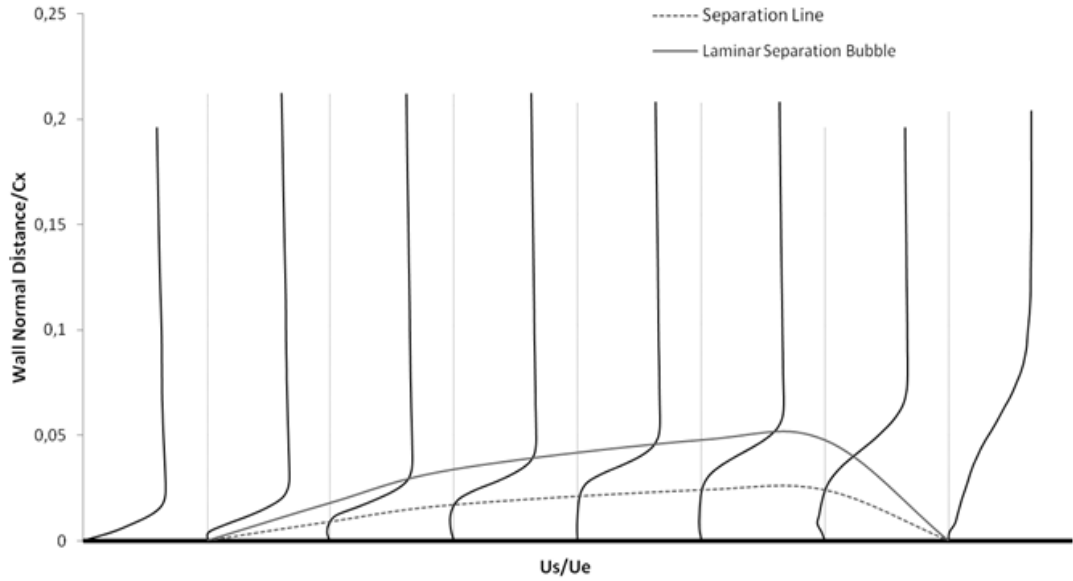


Figure 3.1.11: Laminar separation bubble obtained from velocity profiles

Boundary layer integral quantities are calculated for the baseline case according to definitions given in the following equations.

Displacement thickness:
$$\delta^* = \int_0^{\infty} \left(1 - \frac{U_s}{U_e}\right) dy \quad (\text{Eqn. 3.1})$$

Momentum thickness:
$$\theta = \int_0^{\infty} \frac{U_s}{U_e} \left(1 - \frac{U_s}{U_e}\right) dy \quad (\text{Eqn. 3.2})$$

where U_s is the streamwise velocity, U_e is the local edge velocity and dy is the normal distance to the blade surface. The wall ($y=0$) and the point of maximum velocity, i.e. local edge velocity, are taken as the limits of integration.

The development of boundary layer integral quantities is illustrated in Figure 3.1.12:

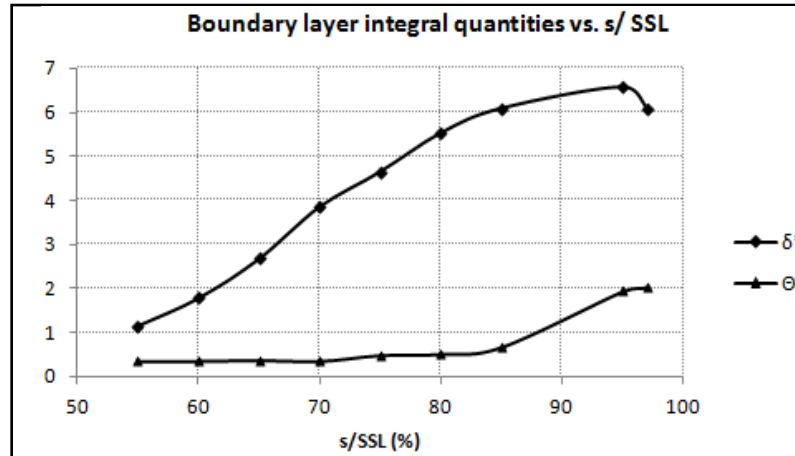


Figure 3.1.12: Displacement and momentum thickness values at different s/SSL stations at $z/d=0$, $B=0$, $Re=29k$.

The low values of momentum thickness until 80% SSL gives information about the transition point. At the beginning, the boundary layer separates due to momentum deficit in the boundary layer and that is represented by these low values. Transitioning to turbulence increases momentum thickness and reattaching as turbulent results in an almost stable value. Displacement thickness grows faster than the momentum thickness. At 55% SSL, the momentum thickness value is lower than the displacement thickness which is typical for a laminar boundary layer. Increase in the displacement thickness can be accounted for boundary layer thickening due to laminar separation and the decrease after around 95% SSL can be explained by reattachment as turbulent. The sharp decrease in the displacement thickness can be accounted for being almost the end of the shear layer at the trailing edge where the displacement thickness values will be very low due to being a boundary-free flow.

The shape factor is calculated as the ratio of the displacement thickness to the momentum thickness. The shape factor represents the existence of adverse pressure gradient in a flow. The smaller shape factor values are favoured implying higher momentum exchange between the fluid particles closer to the wall and the ones further away from the wall. High streamwise momentum of the flow close to wall

augments the flow resistance to adverse pressure gradients. Therefore shape factor is important to determine the susceptibility of the flow to separation. Figure 3.1.13 shows the shape factor values for the specified stations of velocity profiles.

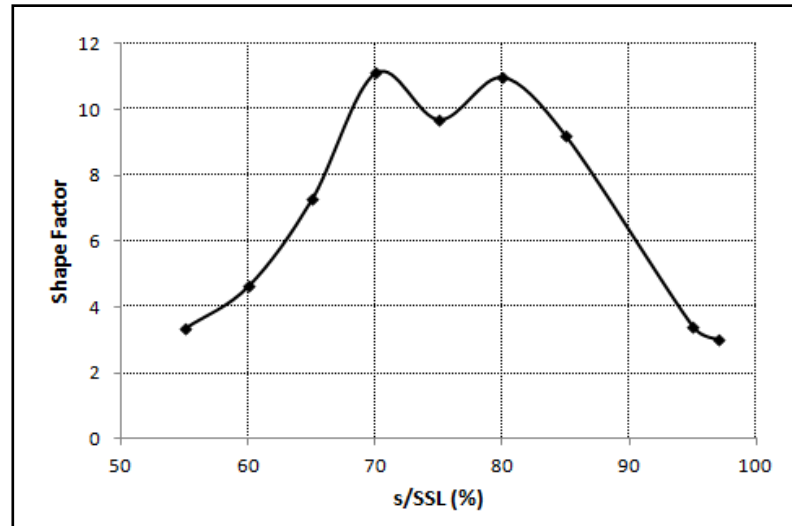


Figure 3.1.13: Shape factor values at different s/SSL stations at $z/d=0$, $B=0$, $Re=29k$.

The increase in shape factor indicates the existence of adverse pressure gradient that results in separation. This sharp increase in the shape factor is an indicative of separation. Also, for a laminar boundary layer, shape factor values greater than 3.8 or 4 indicate a possible separation and a value of 10 and higher are even possible in the separated zone [28]. These values are just for reference because in the literature these values are given for zero pressure gradient case which is not possible for a passage flow in a linear cascade. The shape factor, in our case, increases to a maximum value of around 11 at around 70% SSL which represents the start of the transition. McAuliffe and Yaras [29] stated in their paper that transition starts at the station where the peak shape factor occurs. In addition, TKE contour plots and Reynolds shear stress contour plots (Figure 3.1.4 and Figure 3.1.6, respectively) clearly show the changing flow quantities for that location which also supports the idea. Shape factor values are reduced to a final value once reached to 95% SSL. This reattachment value being almost 3.5 is consistent with Horton's work [30]. The last

two stations in the plot have shape factor values close to each other indicating the flow is reattached and a fully turbulent flow is being developed.

Normalized Reynolds stress components per unit mass are presented in Figure 3.1.14.

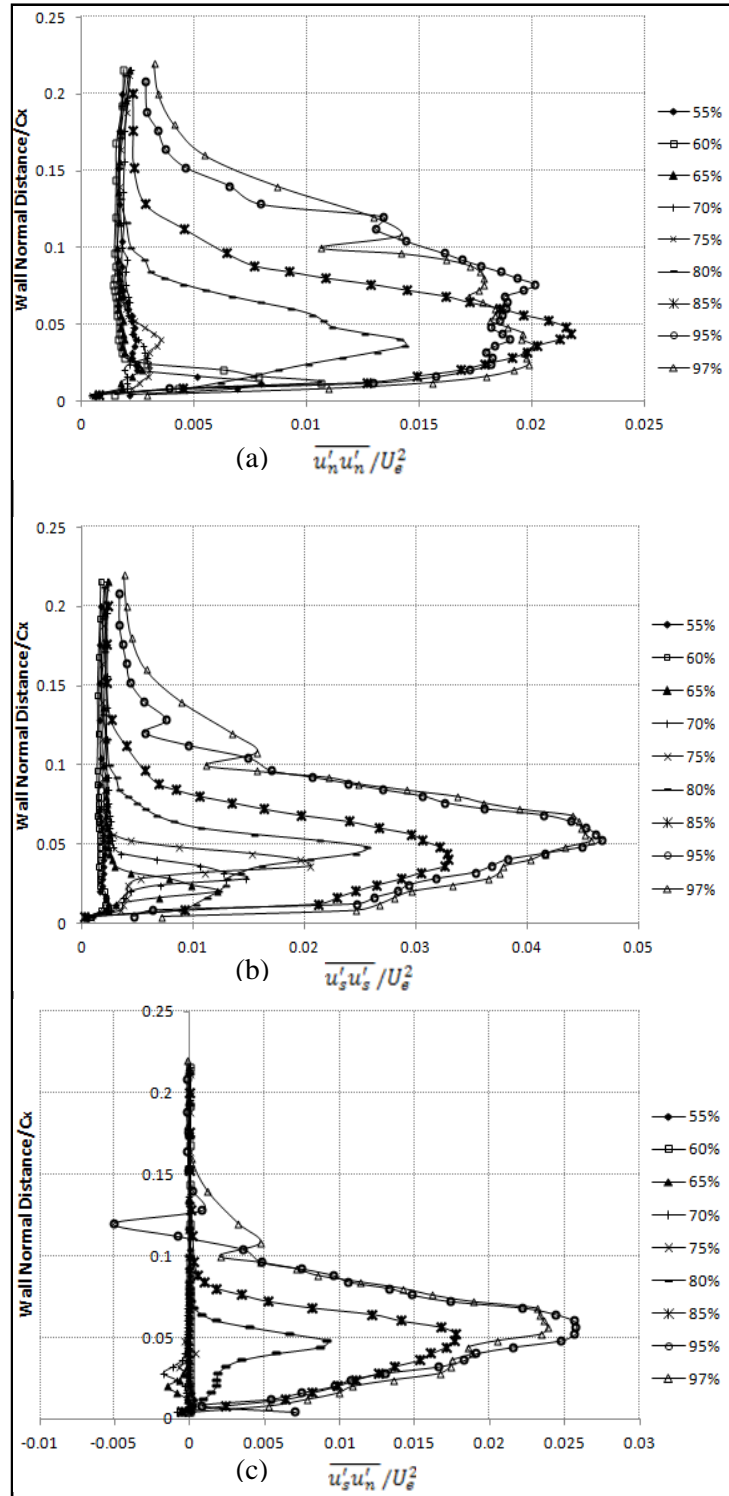


Figure 3.1.14: Normalized Reynolds stress components at specified SSL locations (a) Reynolds normal stresses, $\overline{u'_n u'_n} / U_e^2$ (b) Reynolds normal stresses, $\overline{u'_s u'_s} / U_e^2$, (c) Reynolds shear stresses, $-\overline{u'_s u'_n} / U_e^2$. At $z/d=0$, $B=0$, $Re=29k$.

Reynolds stress components give valuable information about the onset of transition. Specifically, Reynolds shear stresses are responsible for the transport of the momentum into the boundary layer which forces the separated shear layer to reattach [30]. From Figure 3.1.14 (c), Reynolds shear stress, $-\overline{u'_s u'_n} / U_e^2$, is seen to have greater values starting from 80% SSL. From what is stated above, 80% SSL can also be considered as the onset of transition although from shape factor results 70% SSL is said to be the possible transition starting point; but still shape factor values of the stations 70% SSL and 80% SSL are close to each other. It is for sure that transition point is not easily distinguishable. Wall normal stresses ($\overline{u'_n u'_n} / U_e^2$) from Figure 3.1.14 (a) are compatible with the literature showing that high fluctuations occur in the wall normal direction around the reattachment point [31]. For $\overline{u'_s u'_s} / U_e^2$, since this quantity shows the momentum transport in the streamwise direction, it is reasonable to be in an increasing manner starting from separation until reattachment point and the peak occurring at the reattachment point.

3.2 Steady Vortex Generator Jet (VGJ) Cases

Velocity and Turbulence Field Results

After the baseline case has been analyzed and discussed in detail, the effects of steady VGJ blowing can be more easily identified. The jets are injected into the flow from 50% SSL location with 30° pitch and 45° skew angle. The details of VGJ configuration and the measurement details can be found in Chapter 2.

Contour plots presenting the steady VGJ blowing measurements in comparison with baseline case are presented from Figure 3.2.1 to Figure 3.2.5.

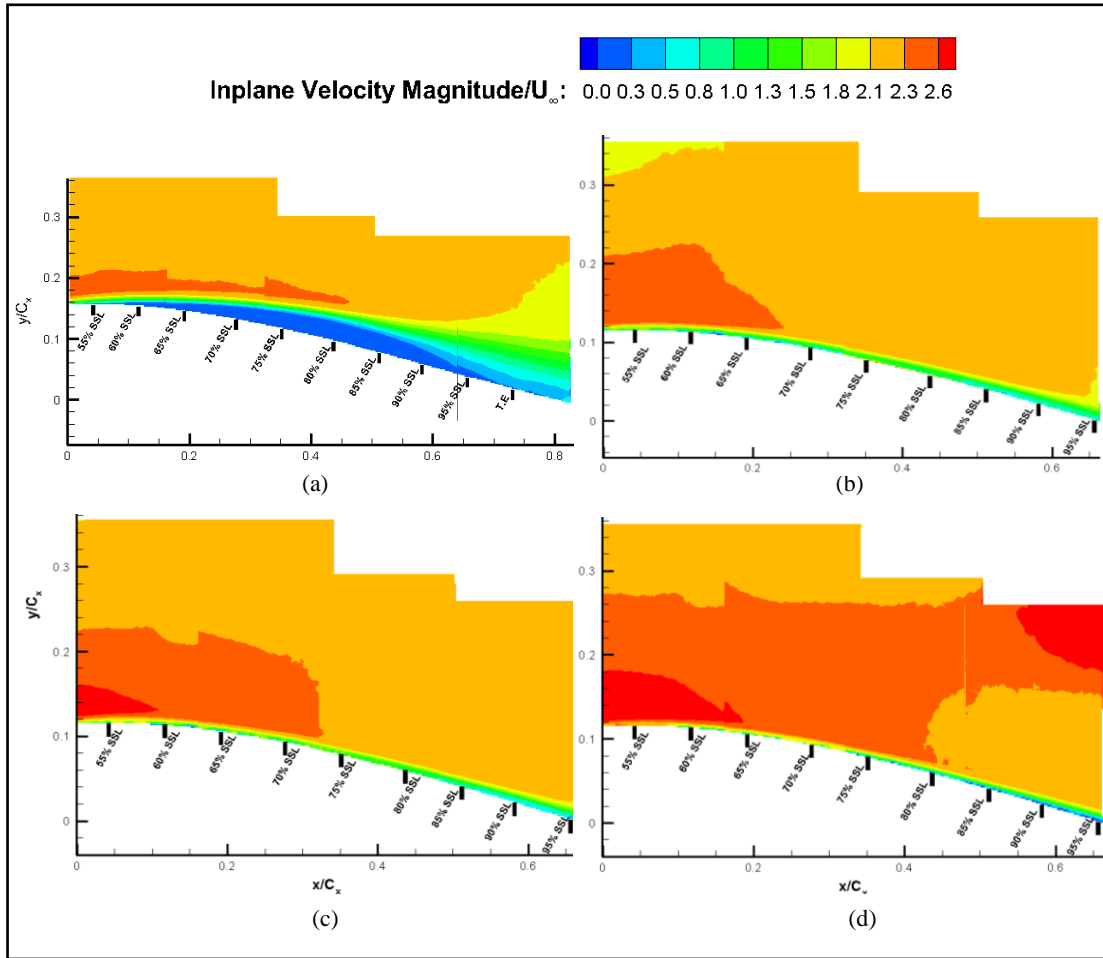


Figure 3.2.1: In-plane mean velocity magnitude/ U_∞ contours at $z/d=0$ showing the aft portion of the blade (55% SSL-Trailing Edge (TE)). (a) $B=0$ (b) $B=2.2$ (c) $B=4.4$ (d) $B=7.2$. The flow is from left to right, $Re=29k$

From in-plane mean velocity magnitude contours, the large separation bubble of the baseline case is seen to be eliminated. For increasing blowing ratios, the boundary layer gets thinner that is more suppressed by the high injection velocities. Having a thinner boundary layer can also be attributed to the fact that turbulent characteristic of the flow is increasing. Since the injection location is at 50% SSL, the jet injection effect on mean velocity distribution can be seen starting from 55% SSL with high in-plane velocity magnitudes. For $B=7.2$ case, the high levels of velocity magnitudes dominating the flow field may be the result of the high blowing ratio. This effect can also be found in the literature ([13], [16]). Sondergaard et al. [13] states that for the

jet injections upstream of the separation location near the peak suction, a blowing ratio ($B=U_{jet}/U_{loc}$, loc: local blade midchannel conditions) above 3 results in strong jets blowing off the boundary layer and rise in losses. According to their B definition, our $B=7.2$ case makes up a blowing ratio of around 3.5. There is no measured evidence about losses in the flow over the suction side boundary layer of the blade for our case but the high levels of turbulent kinetic energy at the locations where the jet crosses the measurement plane outside the boundary layer may cause local pressure losses at the crossing location. This possibility found in the literature should be kept in mind before implementing blowing ratios that high. Turbulent kinetic energy contour plots can be seen Figure 3.2.2.

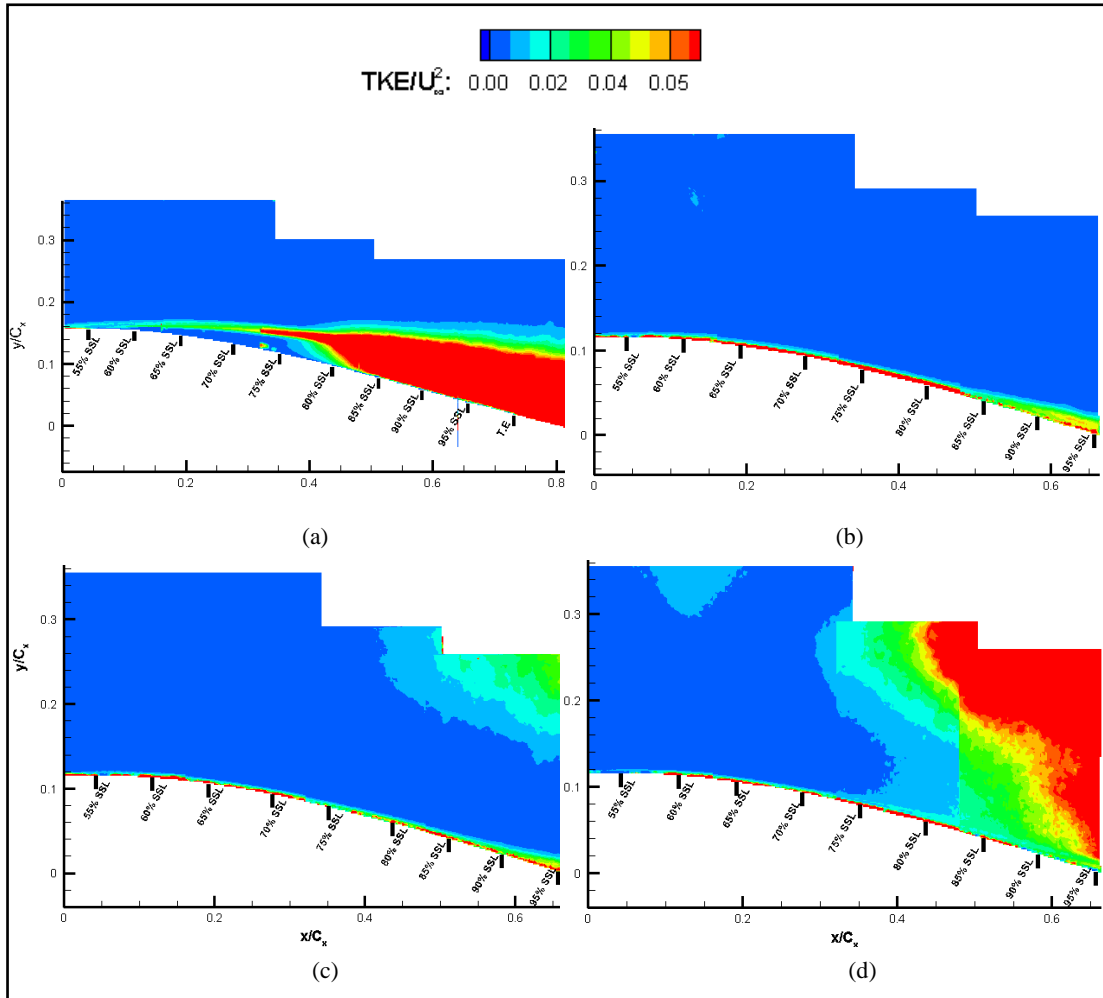


Figure 3.2.2: Turbulent kinetic energy/ U_∞^2 contours at $z/d=0$ showing the aft portion of the blade (55% SSL-Trailing Edge (TE)). (a) $B=0$ (b) $B=2.2$ (c) $B=4.4$ (d) $B=7.2$. The flow is from left to right, $Re=29k$

Since the jets are injected in not only pitched but also in a skewed manner and in a counter-rotating configuration, the jet itself cannot be directly seen in the measurement window. However, the angled jets collide with each other at various locations. For $z/d=0$ measurement plane, two collision locations exist, one is above around 62% SSL and the other is above around 83% SSL. Also, TKE contour plots support these collision locations with high TKE levels becoming more evident by increased blowing ratio.

Reynolds shear stress per unit mass contour plots are given for each injection case in Figure 3.2.3.

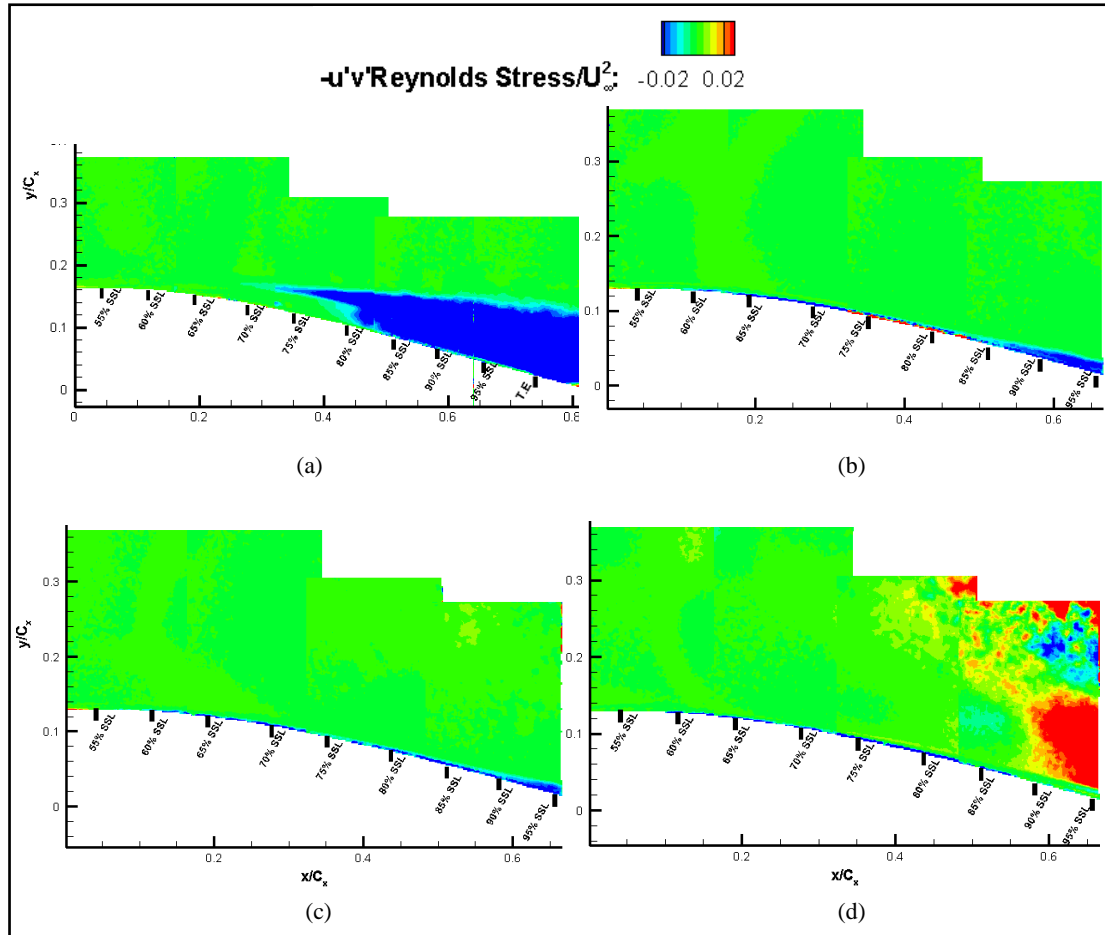


Figure 3.2.3: $-\overline{u'v'}/U_\infty^2$ contours at $z/d=0$ showing the aft portion of the blade (55% SSL-Trailing Edge (TE)). (a) $B=0$ (b) $B=2.2$ (c) $B=4.4$ (d) $B=7.2$. The flow is from left to right, $Re=29k$

Thinning of the boundary layer with the increasing blowing ratio is also evident by Reynolds shear stress contours. The shear stress levels increase with increasing blowing ratio at the locations where the jets cross the measurement plane. This crossing jet effect is parallel with TKE contour plots as explained above.

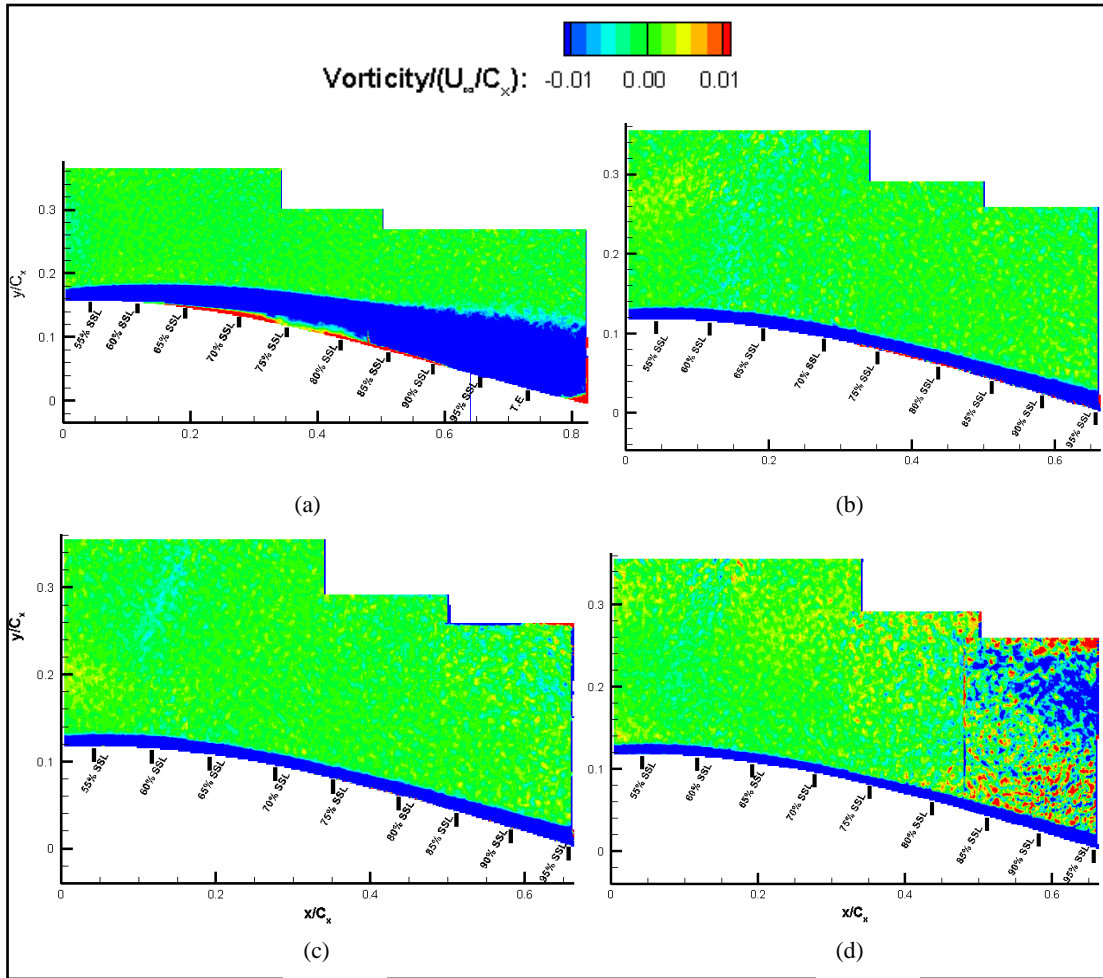


Figure 3.2.4: Non-dimensional mean vorticity, $\Omega_z / (U_\infty / C_x)$, contours at $z/d=0$ showing the aft portion of the blade (55% SSL-Trailing Edge (TE)). (a) $B=0$ (b) $B=2.2$ (c) $B=4.4$ (d) $B=7.2$. The flow is from left to right, $Re=29k$

Vorticity plots are expected to give the physical information about the flow control since this is a vortex generating jet type control. At mid-span ($z/d=0$) plane, vorticity production is not that visible in low blowing ratios. Only in $B=7.2$ case, pairs of vortices generated are seen. To be able to comment more on that, different plane measurement results are presented for mean vorticity contours at $B=2.2$.

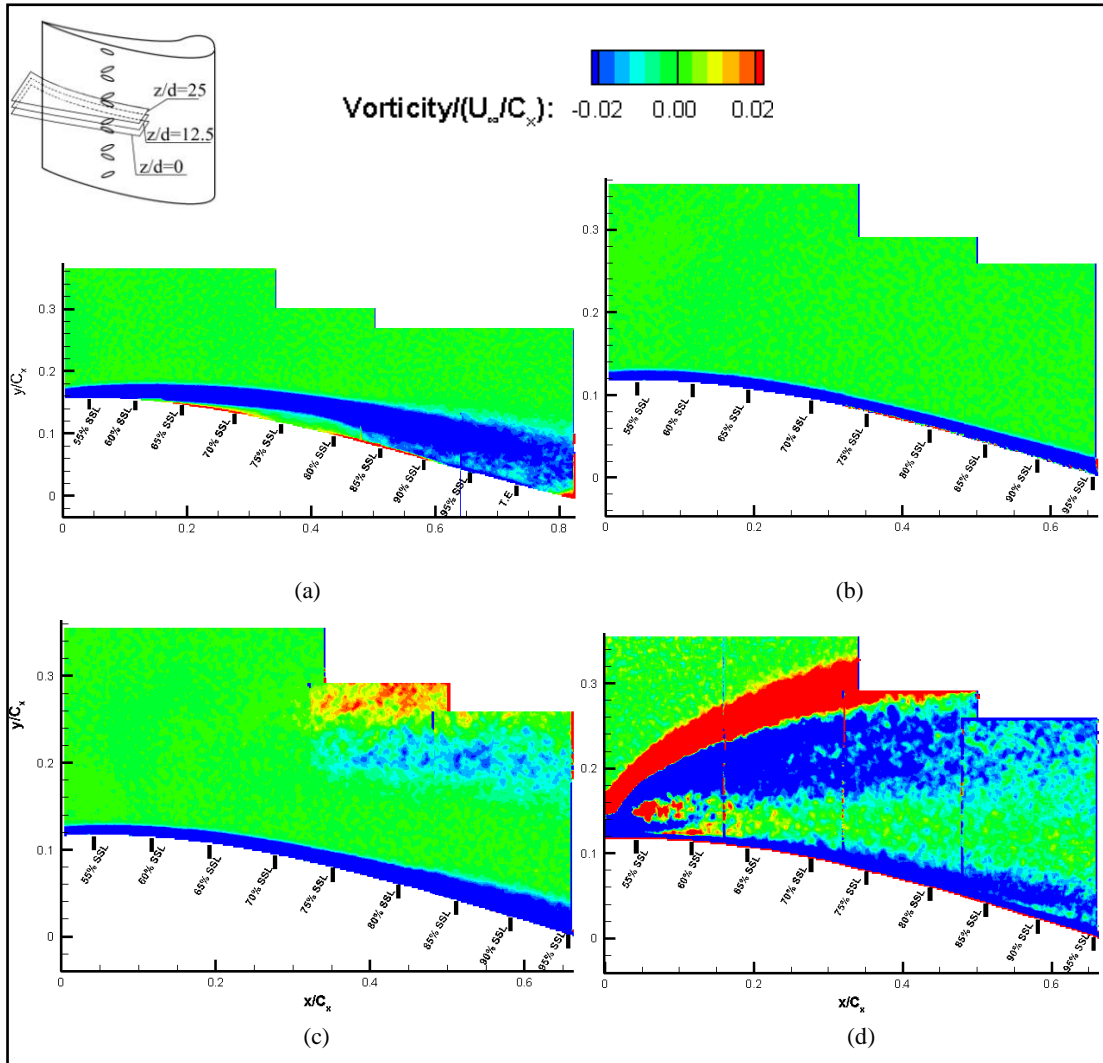


Figure 3.2.5: Non-dimensional mean vorticity, $\Omega_z/(U_\infty/C_x)$, contours showing the aft portion of the blade (55% SSL-Trailing Edge (TE)). (a) $z/d=0$, $B=0$. Injection cases ((b), (c), (d)) are at $B=2.2$. (b) $z/d=0$ (c) $z/d=12.5$ (d) $z/d=25$. The flow is from left to right, $Re=29k$

Starting from $z/d=12.5$ plane, the structures responsible for the suppression of separation bubble are apparent. The angled jets create a double vortex in opposite directions. These are the two legs of horseshoe vortex generated by the injected jets. These streamwise vortices are responsible for mixing between the freestream and the boundary layer. Momentum in the boundary layer is increased through freestream entrainment provided by these streamwise vortices. Therefore, the boundary layer

becomes more resistant to separation. Only single jets are crossing the $z/d=12.5$ plane. These are the jets crossing the plane without any interaction with another jet at the crossing location. At $z/d=25$ plane, there are interacting jets, i.e. two jets directed to each other according to their skew angle colliding at the measurement plane. The directions of the jets can be confirmed again by Figure 2.2.4. Therefore, one can see one pair of vortex in single jet crossing plane and two pairs in interacting jets crossing plane. At $z/d=25$, the jets are interacting at the onset of the measurement windows and since this plane is the midway between two counter-rotating jets, the effects are more dominantly seen. The high levels of vorticity are generated by the streamwise vortices and they are seen to decay in the streamwise direction. Boundary layer profile differences among different measurement planes can be explained by the fact that each measurement plane is differently affected by the jets crossing.

Boundary Layer Analysis

Velocity profiles at specified stations can also give valuable information about the elimination of separation bubble with steady VGJ blowing. The information gathered from velocity profiles will give more ideas about the characteristics of the boundary layer after jet injection.

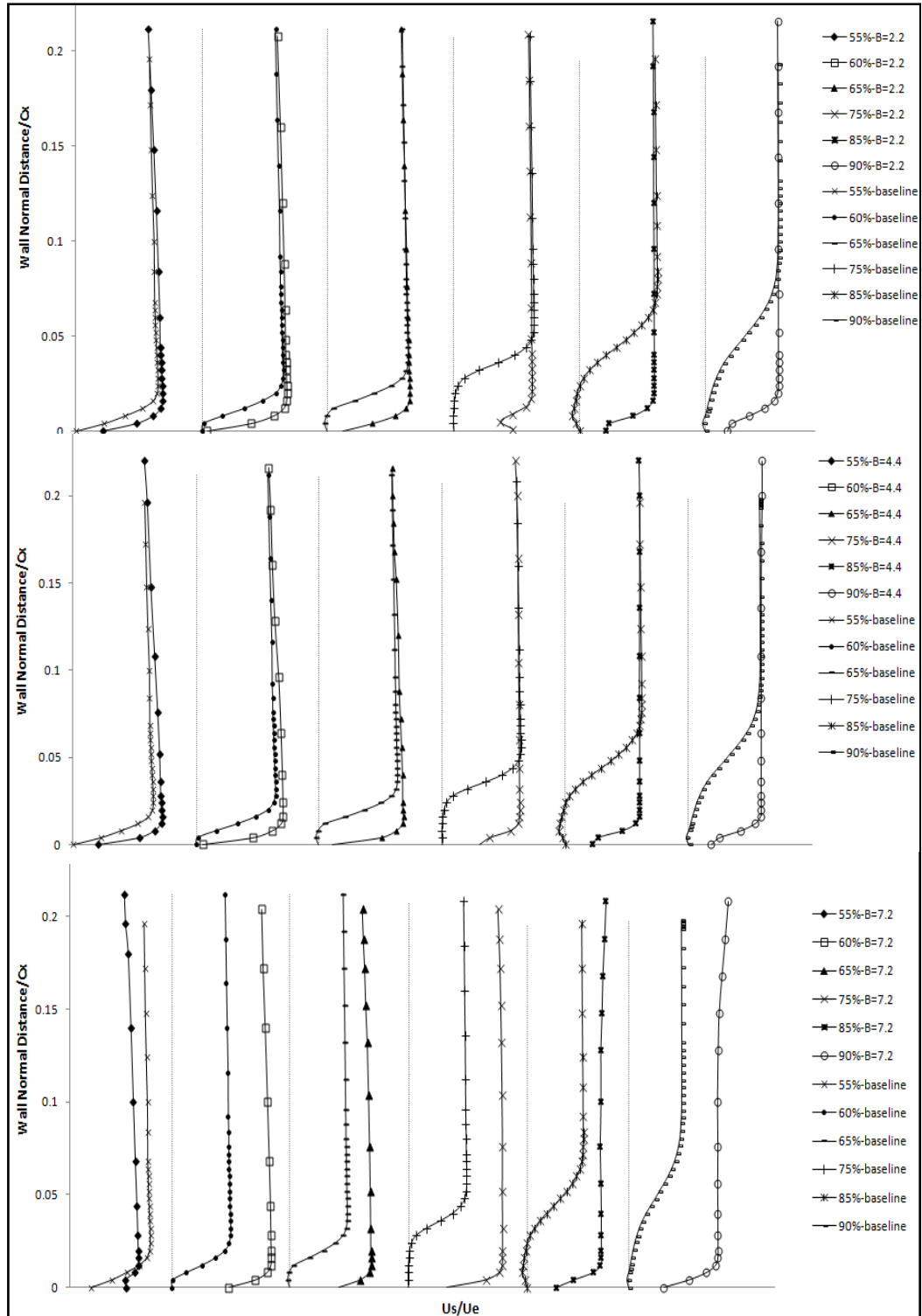


Figure 3.2.6: Boundary layer profiles of mean streamwise velocity normalized by mean edge velocity; profiles at different s/SSL stations at $z/d=0$ for (a) $B=2.2$, (b) $B=4.4$, (c) $B=7.2$, $Re=29k$.

Figure 3.2.6 shows the effectiveness of flow control. It should be kept in mind that in the baseline case, the laminar separation started at 60% SSL station and the bubble length was 35% SSL.

For all injection cases, it can be observed that velocity values are all positive compared to separated case. For $B=2.2$, the boundary layer seems attached at least until a station between 65% and 75% SSL. Since the velocity profile at 85% SSL is similar to a typical reattachment station's velocity profile and 90% SSL is a typical of developing boundary layer profile, then the boundary layer with $B=2.2$ injection may be said to have a very thin separation zone. This is also supported by the typical velocity profile of 75% SSL which is under the effect of an adverse pressure gradient. However, this adverse pressure gradient effect may not be that detrimental, even may not cause any separation but just a recovery from the adverse pressure gradient effect which can be seen as reattachment point. The reason that the contour plots do not show any sign for separation may also be the result of having a very thin separation zone; but still $B=2.2$ injection can be said to be effective to remove that thick and long laminar separation bubble even if it causes a very thin separation zone.

For $B=4.4$, although no adverse pressure gradient is detected at specified stations, 85% SSL may be a reattachment point of the boundary layer which may have separated between 75% SSL and 85% SSL. Still, it can be said that a very thin separation zone occurs but more retarded than the one in $B=2.2$ case. It is thinner than the possible one in $B=2.2$ case; therefore it is still not detectable in contour plots. For $B=7.2$ case, the boundary layer seems fully attached and developing as a turbulent boundary layer. At 55% SSL station, the steep velocity profile can be attributed to the fact that the jet ejection velocity is very high at that blowing ratio; therefore it is expected to have this kind of abnormalities there. In addition, for $B=7.2$ case, the edge velocities are much different than the baseline case which is also the result of blowing at such a high rate.

Boundary layer integral quantities for the smallest injection case in comparison with baseline case are given in Figure 3.2.7.

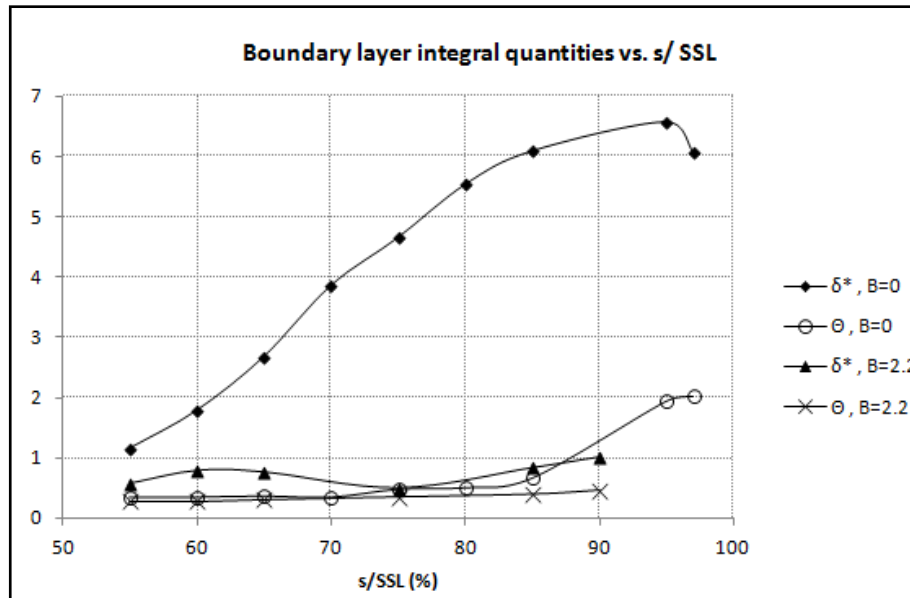


Figure 3.2.7: Displacement and momentum thickness comparison at $z/d=0$, $Re=29k$.

Boundary layer integral quantities are almost constant when compared with the baseline case where laminar separation bubble occurred. If there were a sharp increase in displacement thickness, it would be for sure that the separation occurs for the injection case too; but the small fluctuations in displacement thickness can be the result of the very thin separation zone discussed above with velocity profiles.

Shape factor comparison between the controlled ($B=2.2$) and baseline cases are also made.

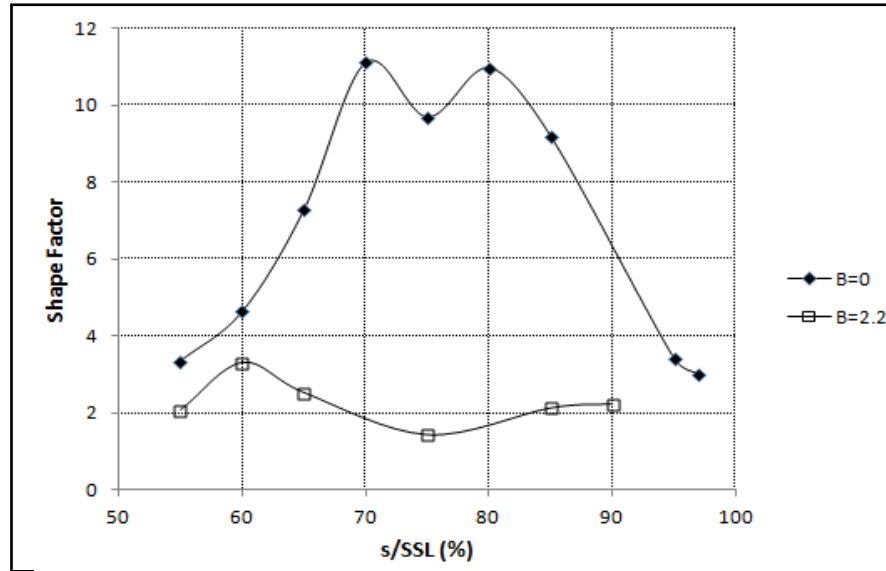


Figure 3.2.8: Shape factor comparison for B=0 and B=2.2 at $z/d=0$, $Re=29k$.

Almost constant shape factor values also suggest that there is no separation. However, similar to displacement thickness behaviour, a very thin separation zone can be the reason for the fluctuations in shape factor values. Also the values staying comparably low is an indication of developing turbulent boundary layer created after jet blowing.

Total Pressure Measurements

Total pressure measurements are performed in order to comment on losses both for controlled and uncontrolled cases. These measurements are helpful to observe the effectiveness of the flow control and the effect of high blowing ratio injections on pressure losses.

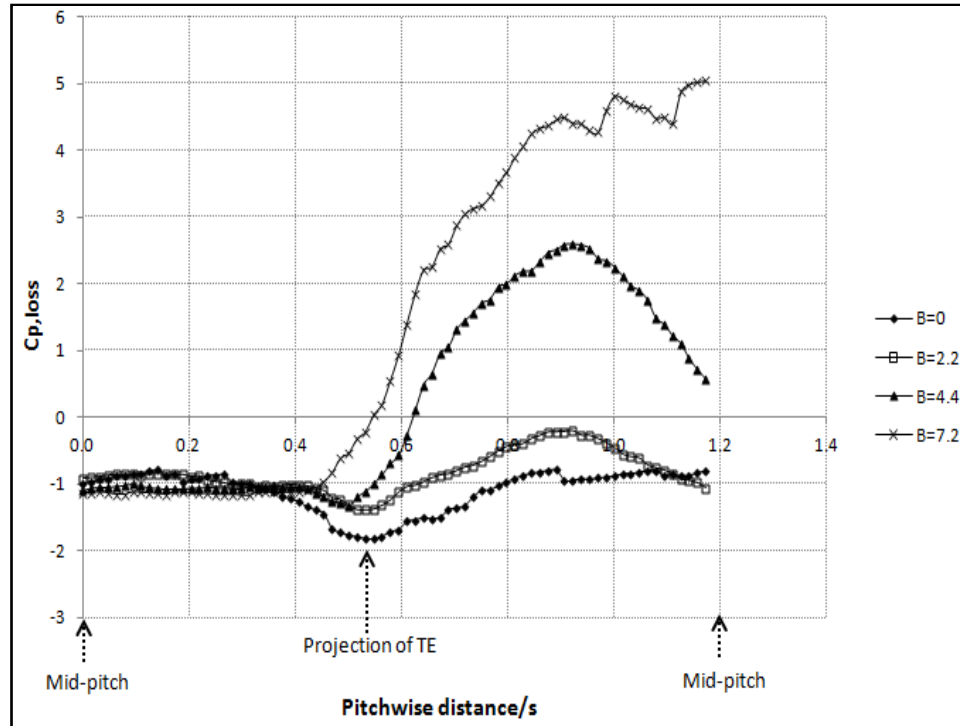


Figure 3.2.9: Pitchwise total pressure loss coefficient variation at midspan, $0.5C_x$ downstream of the blade row for baseline ($B=0$) and three injection cases

These measurements encompass around one pitch distance from the mid-pitch location of the test blade and the neighbouring blade on the pressure side to the mid-pitch location of the test blade and the neighbouring blade on the suction side as described in the measurement details section in Chapter 2. For $B=0$ case, the increase in the loss coefficient indicates the wake of the test blade. For $B=2.2$, these losses are effectively reduced evident by the reduction in the peak loss. For $B=4.4$ case, the jet persists downstream of the trailing edge and results in a positive total pressure loss peak [32]. For the highest blowing case studied, $B=7.2$, this increase is even more severe and this may support the studies suggesting that the jets injected at very high blowing ratios may dominate the flow and even cause pressure losses [13], [16]. Although there is no problem in repeatability of the measurements since four cases coincide at the beginning, the values achieved there are open to discussion and should be repeated in order to obtain expected results of around 0 [18].

CHAPTER 4

CONCLUSION

4.1 General Conclusions

In this thesis, the effects of steady vortex generator jets on laminar boundary layer separation occurring on the suction side of a low pressure turbine (LPT) blade at low Reynolds numbers are investigated. For this purpose, a linear cascade model of five T106 LPT blades is used in a low speed blower configuration wind tunnel. The test blade, which is the mid blade in the cascade model, is first instrumented with pressure taps at mid span in order to define the separation problem with corresponding pressure distribution. Then, the flow control embedded test blade is designed and manufactured. The vortex generator jets (VGJs) are configured at 30° pitch and 45° skew angle. The jets are issued from upstream of the separation location near the suction peak of the blade. Particle Image Velocimetry (PIV) measurements are performed for both controlled and uncontrolled cases. Uncontrolled case is investigated in detail to be able to define the boundary layer separation problem properly.

A long laminar separation bubble occurred on the aft portion of the turbine blade. Separated shear layer reattached to the blade surface near the trailing edge. One point to mention here is that the laminar-to-turbulent transition started over the bubble but then merged into the bubble close to boundary probably due to boundary layer

entrainment by freestream. Controlled cases are performed at three different blowing ratios. Steady VGJs are observed to create streamwise vortices that are found to be responsible for the prevention of the separation. The long separation bubble can be said to be suppressed through steady injection. A complete elimination of the laminar separation bubble, however, is discussed for each injection scenario. At the lowest blowing ratio tested, a very thin separation zone is detected. The separation can be said to be retarded and also the pressure losses are observed to decrease compared to uncontrolled case. The highest blowing ratio tested allowed a fully-attached, developing turbulent boundary layer but the pressure losses associated with the high blowing rates are observed during local total pressure loss measurements. The only parameter that is tested during the study, the blowing ratio, should be chosen accordingly before implementing this method to a real life problem.

4.2 Recommendations for Further Research

This experimental study can also be performed for a pulsed type vortex generator jet to be able to discuss the efficiency of the method tested in this study. Since the first aim was to study fluidic oscillator that is to be embedded in the turbine blade to create periodically pulsed jets, this can be achieved through reviewing the fluidic oscillator embedded turbine blade design and also doing numerical simulations for oscillation before manufacturing is very crucial. A cleaner manufacturing may enable to realize that aim which will be a valuable state-of-the-art study.

This study is like a pilot study to prove the capability of the facility in Aerospace Engineering Department to show that the boundary layer measurements can be performed through PIV measurements and the results consistent with the literature show that the data are reliable. The phenomena related to this work can further be studied both theoretically and experimentally.

REFERENCES

- [1] Wisler, D. C. (1998). The Technical and Economic Relevance of Understanding Boundary Layer Transition in Gas Turbine Engines. Minnowbrook II - Workshop on Boundary Layer Transition in Turbomachines, NASA/CP-1998-206958.
- [2] Hodson, H., Huntsman I., & Steele, A. B. (1994). An Investigation of Boundary Layer Development in a Multistage LP Turbine. *J. of Turbomachinery*, 116, 375-383.
- [3] Zhang, X. F. (2005). Separation and Transition Control on Ultra-High-Lift Low Pressure Turbine Blades in Unsteady Flow. PhD Thesis. Cambridge University.
- [4] Zoric, T., Popovic, I., Sjolander, S. A., Praisner, T., & Grover, E. (2007). Comparative Investigation of Three Highly Loaded LP Turbine Airfoils: Part 1- Measured Profile and Secondary Losses at Design Incidence. GT2007-27537.
- [5] Sharma, O. P., Ni, R. H., & Tanrikut, S. (1994). Unsteady Flows in Turbines- Impact on Design Procedure. In AGARD-LS-195.
- [6] Horton, H.P. (1968). Laminar Separation Bubbles in Two and Three-dimensional Incompressible Flow. PhD Thesis. Univ. London, UK.
- [7] Sandham, N. D. (2008). Transitional Separation Bubbles and Unsteady Aspects of Aerofoil Stall. *The Aeronautical J.* July issue, Vol. 112, No. 1133.
- [8] Volino, R. J. (2003). Passive Flow Control on Low-Pressure Turbine Airfoils. ASME Paper No. GT2003-38728. Atlanta, Georgia.

- [9] Lake, J. P., King, P. I., & Rivir, R. B. (2000). Low Reynolds Number Loss Reduction on Turbine Blades with Dimples and V-Grooves. AIAA paper No. 00-0738. AIAA 37th Aerospace Sciences Meeting & Exhibit. Reno, NV.
- [10] Postl, D. (2005). Numerical Investigation of Laminar Separation Control Using Vortex Generator Jets. PhD Thesis. Univ. Arizona.
- [11] Johari, H., & Rixon, G. S. (2003). Effects of Pulsing on a Vortex Generator Jet. AIAA Journal, Vol. 41, No. 12, 2309-2315.
- [12] Johnston, J. P., & Nishi, M. (1990). Vortex Generator Jets: Means for Flow Separation Control. AIAA Journal, Vol. 28, No. 6.
- [13] Sondergaard, R., Rivir, R. B., & Bons, J. (2002). Control of Low Pressure Turbine Separation Using Vortex Generator Jets. Journal of Propulsion and Power, Vol. 18, No. 4.
- [14] Compton, D. A., & Johnston, J. P. (1994). Streamwise Vortex Production by Pitched and Skewed Jets in a Turbulent Boundary Layer. AIAA Journal, Vol. 30, No. 12.
- [15] Volino, R. J., Kartuzova, O., & Ibrahim, M. B. (2011). Separation Control on a Very High Lift Low Pressure Turbine Airfoil Using Pulsed Vortex Generator Jets. Journal of Turbomachinery, Vol. 133.
- [16] McQuilling, M., & Jacob, J. (2004). Effect of Chord Location on Separation Control with Vortex Generator Jets on Low Pressure Turbine Blades. 2nd Flow Control Conference, AIAA 2004-2205.
- [17] Hansen, L., & Bons, J. (2006). Flow Measurements of Vortex Generator Jets in Separating Boundary Layer. Journal of Propulsion and Power, Vol. 22, No. 3.
- [18] Mercan, B. (2012). Experimental Investigation of the Effects of Waveform Tip Injection on the Characteristics of Tip Leakage Vortex in a LPT Cascade. MSc Thesis. METU.
- [19] Shaw, R. (1959). The Influence of Hole Dimensions on Static Pressure Measurements. University of Liverpool.

- [20] Huang, R. F., & Chang, K. T. (2007). Evolution and Turbulence Properties of Self-Sustained Transversely Oscillating Flow Induced by Fluidic Oscillator. *Transactions of the ASME*, Vol. 129.
- [21] Khan, Z. U., & Johnston, J. P. (2000). On Vortex Generating Jets. *International Journal of Heat and Fluid Flow*, Vol. 21, No. 5, 506-511.
- [22] Mercan, B., Ostovan, Y., Doğan, E., & Uzol, O. (2010). Effect of Chordwise Modulated Waveform Tip Injection on the Characteristics of the Tip Vortex. 40th Fluid Dynamics Conference and Exhibit. Chicago. June 28-July 1.
- [23] Uzol, O., Brzozowski, D., Chow, Y. C., Katz, J., Meneveau, C. (2007). A Database of PIV Measurements within a Turbomachinery Stage and Sample Comparisons with Unsteady RANS. *Journal of Turbulence*, Vol. 8.
- [24] Von Ellenrieder, K. D., & Pothos, S. (2007). PIV Measurements of the Asymmetric Wake of a Two-Dimensional Heaving Airfoil. *Experiments in Fluids*, Vol. 44, No. 5.
- [25] Volino, R. J. (2002). Separated Flow Transition Under Simulated Low-Pressure Turbine Airfoil Conditions - Part 1: Mean Flow and Turbulence Statistics. *Journal of Turbomachinery*, Vol. 124.
- [26] Stieger, R. D. (2002). The Effects of Wakes on Separating Boundary Layers in Low Pressure Turbines. PhD Thesis. Cambridge University.
- [27] Van Ingen, J.L., Boermans, L.M.M. (1985). Research on Laminar Separation Bubbles at Delft University of Technology in Relation to Low Reynolds Number Airfoil Aerodynamics. Proceedings of the Conference on Low Reynolds Number Airfoil Aerodynamics. Notre Dame, Indiana, June.
- [28] The Technische Universität München,
http://www.aer.mw.tum.de/fileadmin/tumwaer/www/pdf/lehre/grenzschicht/lectures/lecture_03.pdf, last visited on June 11th, 2012.

- [29] McAuliffe, B. R., & Yaras, M. I. (2005). Separation-Bubble-Transition Measurements on a Low-Re Airfoil Using Particle Image Velocimetry. ASME Turbo Expo 2005: Power for Land, Sea, and Air, GT2005-68663, 1029-1038.
- [30] Horton, H. P. (1969). A Semi-empirical Theory for the Growth and Bursting of Laminar Separation Bubbles. Aeronautical Research Council CP 1073.
- [31] Burgmann, S., Dannemann, J., & Schröder, W. (2008). Time-resolved and Volumetric PIV Measurements of a Transitional Separation Bubble on an SD7003 Airfoil. Experiments in Fluids, Vol. 44, 609-622.
- [32] McAuliffe, B. (2003). An Experimental Study of Flow Control Using Blowing For a Low-Pressure Turbine Airfoil. MSc Thesis. Carleton University.